

GLACE survey: OSIRIS/GTC Tuneable Filter $H\alpha$ imaging of the rich galaxy cluster ZwCl 0024.0+1652 at $z = 0.395$

Part I – Survey presentation, TF data reduction techniques and catalogue

M. Sánchez-Portal^{1,2}, I. Pintos-Castro^{3,4,8,2}, R. Pérez-Martínez^{1,2}, J. Cepa^{4,3}, A. M. Pérez García^{3,4}, H. Domínguez-Sánchez²⁹, A. Bongiovanni^{3,4}, A. L. Serra²³, E. Alfaro⁵, B. Altieri¹, A. Aragón-Salamanca⁶, C. Balkowski⁷, A. Biviano⁹, M. Bremer¹⁰, F. Castander¹¹, H. Castañeda¹², N. Castro-Rodríguez^{3,4}, A. L. Chies-Santos²⁵, D. Coia¹, A. Diaferio^{23,24}, P.A. Duc¹³, A. Ederoclite²¹, J. Geach¹⁴, I. González-Serrano¹⁵, C. P. Haines¹⁶, B. McBreen¹⁷, L. Metcalfe¹, I. Oteo^{26,27}, I. Pérez-Fournón^{4,3}, B. Poggianti¹⁸, J. Polednikova^{3,4}, M. Ramón-Pérez^{3,4}, J. M. Rodríguez-Espinoza^{4,3}, J. S. Santos²⁸, I. Smail¹⁹, G. P. Smith¹⁷, S. Tempurin²⁰, and I. Valtchanov¹

(Affiliations can be found after the references)

Received; accepted

ABSTRACT

Context. The cores of clusters at $0 \lesssim z \lesssim 1$ are dominated by quiescent early-type galaxies, whereas the field is dominated by star-forming late-type galaxies. Clusters grow through the accretion of galaxies/groups from the surrounding field, which implies that galaxy properties, notably the star formation ability, are altered as they fall into overdense regions. The critical issues to understand this evolution are how the truncation of star formation is connected to the morphological transformation and what physical mechanism is responsible for these changes. The GaLAXy Cluster Evolution Survey (GLACE) is conducting a thorough study on the variation of galaxy properties (star formation, AGN activity and morphology) as a function of environment in a representative and well-studied sample of clusters.

Aims. To address these questions, the GLACE survey is performing a deep panoramic survey of emission line galaxies (ELG), mapping a set of optical lines ([O II], [O III], $H\beta$ and $H\alpha$ /[N II] when possible) in several galaxy clusters at $z \sim 0.40, 0.63$ and 0.86 .

Methods. Using the Tuneable Filters (TF) of the OSIRIS instrument at the 10.4m GTC telescope, the GLACE survey applies the technique of TF tomography: for each line, a set of images are taken through the OSIRIS TF, each image tuned at a different wavelength (equally spaced), to cover a rest frame velocity range of several thousands km/s centred at the mean cluster redshift is scanned for the full TF field of view of 8 arcmin diameter.

Results. Here we present the first results of the GLACE project, targeting the $H\alpha$ /[N II] lines in the intermediate redshift cluster ZwCl 0024.0+1652 at $z = 0.395$. Two pointings, covering $\sim 2 \times r_{vir}$ have been performed. We discuss the specific techniques devised to process the TF tomography observations in order to generate the catalogue of cluster $H\alpha$ emitters, that contains more than 200 sources down to a star formation rate (SFR) $\lesssim 1 M_{\odot}/\text{yr}$. An ancillary broadband catalogue is constructed, allowing us to discriminate line interlopers by means of colour diagnostics. The final catalog contains 174 unique cluster sources. The AGN population is discriminated using different diagnostics and found to be $\sim 37\%$ of the ELG population. The median SFR of the star-forming population is $1.4 M_{\odot}/\text{yr}$. We have studied the spatial distribution of ELG, confirming the existence of two components in the redshift space. Finally, we have exploited the outstanding spectral resolution of the TF, attempting to estimate the cluster mass from ELG dynamics, finding $M_{200} = (4.1 \pm 0.2) \times 10^{14} M_{\odot} h^{-1}$, in agreement with previous weak-lensing estimates.

Key words. galaxies: clusters: individual: ZwCl 0024.0+1652 – galaxies: photometry – galaxies: star formation – galaxies: active

1. Introduction

It is well known that, while the cores of nearby clusters are dominated by red early-type galaxies, a significant increase in the fraction of blue cluster galaxies is observed at $z > 0.2$ (the so-called Butcher-Oemler -BO- effect; Butcher & Oemler 1984). An equivalent increase in obscured star formation (SF) activity has also been seen in mid- and far- IR surveys of distant clusters (Coia et al. 2005; Geach et al. 2006; Haines et al. 2009; Altieri et al. 2010) as well as a growing population of AGN (e.g. Martini et al. 2009, 2013). In general, a strong evolution (i.e. increase of the global cluster star formation rate –SFR) is observed (e.g. Webb et al. 2013; Koyama et al. 2011).

Even focusing on a single epoch, aspects of this same evolutionary trend have been discovered in the outer parts of clusters where significant changes in galaxy properties can be clearly identified such as gradients in typical colour or spectral proper-

ties with clustercentric distance (Balogh et al. 1999; Pimbblet et al. 2001) and in the morphology-density relation (Dressler 1980; Dressler et al. 1997). In a hierarchical model of structure formation, galaxies assemble into larger systems, namely galaxy clusters, as time progresses. It is quite likely that this accretion process is responsible for a transformation of the properties of cluster galaxies both as a function of redshift and as a function of environment (Balogh et al. 2000; Kodama & Bower 2001).

Haines et al. (2013) measured the mid-IR BO effect over the redshift range $0.0-0.4$, finding a rapid evolution in the fraction of cluster massive ($M_K < -23.1$) luminous IR galaxies within r_{200} and $\text{SFR} > 3 M_{\odot}/\text{yr}$ that can be modeled as $f_{SF} \propto (1+z)^n$, with $n = 7.6 \pm 1.1$. The authors investigate the origin of the BO effect, finding that can be explained as a combination of a $\sim 3\times$ decline in the mean specific-SFR of star-forming cluster galaxies since $z \sim 0.3$ with a $\sim 1.5\times$ decrease in number density. Two-thirds of this reduction in the specific-SFRs of star-forming clus-

ter galaxies is due to the steady cosmic decline in the specific-SFRs among those field galaxies accreted into the clusters. The remaining one-third reflects an accelerated decline in the SF activity of galaxies within clusters. The slow quenching of SF in cluster galaxies is consistent with a gradual shut down of SF in infalling spiral galaxies as they interact with the cluster medium.

Possible physical processes that have been proposed to trigger or inhibit the SF include (e.g. Treu et al. 2003): (i) Galaxy-ICM interactions: ram-pressure stripping, thermal evaporation of the ISM, turbulent and viscous stripping, pressure-triggered SF. When a slow decrease of the SF is produced, these mechanisms are collectively labelled as starvation. (ii) Galaxy-cluster gravitational potential interactions: tidal compression, tidal truncation. (iii) Galaxy-galaxy interactions: mergers (low-speed interactions), harassment (high-speed interactions). Nevertheless, it is still largely unknown whether the correlations of star-formation histories and large-scale structure are due to the advanced evolution in overdense regions, or to a direct physical effect on the star formation capability of galaxies in dense environments (e.g. Popesso et al. 2007). This distinction can be made reliably if one has an accurate measurement of star formation rate (or history), for galaxies spanning a range of stellar mass and redshift, in different environments.

The physical processes proposed above act on the cluster population of emission line galaxies (ELG; comprising both SF and AGN population); narrow-band imaging surveys are very efficient to identify *all* the ELGs in a cluster. For instance, Koyama et al. (2010) performed a MOIRCS narrow-band $H\alpha$ and *Akari* mid-IR survey of the cluster RX J1716.4+6708 at $z=0.81$, showing that both $H\alpha$ and mid-IR emitters avoid the central cluster regions. A population of red SF galaxies (comprising both $H\alpha$ and mid-IR emitters) is found in medium-density environments like outskirts, groups and filaments, suggesting that dusty SF is triggered in the infall regions of clusters, implying a probable link between galaxy transition and dusty SF. The authors found that the mass-normalised cluster SFR declines rapidly since $z \sim 1$ as $\propto (1+z)^6$ (i.e. consistent with the results from Haines et al. 2013, outlined above). “Classical” narrow-band imaging surveys have therefore demonstrated to be a powerful tool, but suffer from ambiguity about the true fluxes of detected sources and do not provide neither accurate membership nor dynamical information about the population. Attempting to overcome these limitations, but taking advantage of the power of narrow-band imaging, the GaLaxy Cluster Evolution Survey (GLACE) has been designed as an innovative survey of ELGs and AGNs in a well-studied and well-defined sample of clusters, exploiting the novel capabilities of tunable filters (TF) of the OSIRIS instrument (Optical System for Imaging and low-Resolution Integrated Spectroscopy; Cepa et al. 2003, 2005) at the 10.4m GTC telescope, to map a set of important optical emission lines by means of the technique of “TF tomography”, scanning a range of the spectrum, i.e. a range of radial velocities around the cluster nominal redshift, at a fixed wavelength step.

The main purpose of this paper is to present the GLACE project, along with some specific techniques devised to process TF data and the results of several simulations performed to assess the quality and performance of the observations and procedures developed. In addition, results from the $H\alpha$ /[N II] survey performed in the galaxy cluster ZwCl 0024+1652 (hereafter referred as Cl0024) at $z=0.395$ are presented. In sect. 2, the GLACE survey is outlined, including its main objectives, technical implementation and intended targets. Then, sect. 3 reports on the observations performed towards Cl0024, along with the procedures developed to reduce TF data within the GLACE sur-

vey. The method for flux calibration is also addressed, as well as Cl0024 ancillary broadband data and spectroscopic redshifts. In sect. 4 the methods to derive the catalogue of ELG, including line wavelength estimation and rejection of contaminants (line emitters at different redshifts) are described. sect. 5 addresses the derivation of the $H\alpha$ and [N II] fluxes and possible explanations to the absorption-like features observed in some cases in the spectral data. In sect. 6 we discuss the spatial and redshift distribution of the cluster galaxies. sect. 7 is dedicated to the $H\alpha$ luminosity function of Cl0024 and its comparison with previous work (Kodama et al. 2004). In sect. 8, the discrimination between star-forming (SF) galaxies and AGNs is discussed. Finally, sect. 9 investigates the possibility of studying the dynamical properties of clusters of galaxies by means of emission (rather than absorption) lines.

This is the first of a series of papers on the GLACE targets. A thorough discussion on the SF properties of Cl0024 derived from the $H\alpha$ line and their comparison with mid- and far-IR results, as well as discussion on the results derived from the rest of lines targeted will be addressed in forthcoming papers (Pérez-Martínez et al., in preparation). The infrared-derived SF properties of the young galaxy cluster RX J1257.2+4738 at $z=0.866$ (see GLACE target list below) have been discussed in Pintos-Castro et al. (2013). The GLACE [O II] OSIRIS TF survey of this cluster and the morphological properties of the SF and AGN population are being addressed in Pintos-Castro et al. (in preparation).

Unless otherwise specified, throughout this paper we assume a Universe with $H_0 = 70 \text{ km s}^{-1} \text{ Mpc}^{-1}$, $\Omega_\Lambda = 0.7$ and $\Omega_m = 0.3$.

2. The GLACE Project

The GLACE programme (PIs. Miguel Sánchez-Portal & Jordi Cepa) is undertaking a panoramic census of the star formation and AGN activity within a sample of clusters at three redshift bins defined by windows relatively free of strong atmospheric OH emission lines (Fig. 1): $z \sim 0.40, 0.63$ and 0.86 , mapping the strongest rest-frame optical emission lines: $H\alpha$ (only at $z \sim 0.4$), $H\beta$, [O II]3727 and [O III]5007; the sections below describe the main goals of the GLACE project and the technical implementation of the project.

2.1. GLACE goals

The GLACE project is aimed at comparing the maps of ELGs with the structures of the targeted clusters (as traced by galaxies, gas and dark matter) to address several crucial issues:

(1) Star formation in clusters: We will determine how the star formation properties of galaxies relate to their position in the large scale structure. This will provide a key diagnostic to test between different models for the environmental influence on galaxy evolution. Each mechanism is most effective in a different environment (generally depending on the cluster-centric distance, e.g. Treu et al. 2003), leaving a footprint in the data. We are mapping the extinction-corrected star formation through $H\alpha$ and [O II], over a large and representative region in a statistically useful sample of clusters. The survey has been designed to reach $\text{SFR} \sim 2 \text{ M}_\odot/\text{yr}$ (i.e. below that of the Milky Way) with 1 magnitude of extinction at $H\alpha$ ¹. Our first results (see sect. 4) show that we are achieving this goal. Another important question that can be addressed is related with the kind of galaxies

¹ $f_{H\alpha} = 1.89 \times 10^{-16} \text{ erg s}^{-1}$ at $z=0.4$ using standard SFR–luminosity conversion factors (Kennicutt 1998)

(type/mass) forming stars within clusters. The study of the morphology of confirmed ELGs allows investigating the connection between the truncation of star formation and the morphological transformation of infalling galaxies (e.g. Poggianti et al. 1999). In addition, by determining the total integrated star formation rates, we can construct a star-formation history for galaxies in clusters, as has been done in the field (e.g. Madau et al. 1998).

(2) The role of AGNs: Whether the fraction of AGNs is environment-dependent or not is a matter of debate: while some results Miller et al. (2003) point towards a lack of dependency of the AGN fraction with the local galaxy density, other authors (e.g. Kauffmann et al. 2004) conclude that high-luminosity AGNs do avoid high-density regions. Such a lack of AGNs in clusters, as compared to the field, may be related to the evolution of galaxies as they enter the cluster environment. On the other hand, claims for an enhanced fraction of AGNs in groups (e.g. Popesso & Biviano 2006) point at AGN-stimulating processes such as galaxy–galaxy interactions or mergers that are particularly effective in the low-velocity dispersion and (relatively) high-density environments typical of groups (and filaments).

Regarding redshift evolution, Martini et al. (2009, 2013) have studied the fraction of luminous AGNs in clusters up to $z \approx 1.5$, finding that it is 30 times greater at $1 < z < 1.5$ than the fraction found in clusters at $z \sim 0.25$ and more than one order of magnitude larger than that found at $z \sim 0.75$, indicating that the AGN population in clusters has evolved more rapidly than the field one, in analogy with the faster evolution of cluster SF galaxies with respect to field.

A complete census of the AGN population in clusters at different redshifts, and in cluster regions characterized by different mean densities and velocity dispersions, can help us to constrain the physics behind the onset of the AGN activity in galaxies. Our survey is sensitive to the AGN population within clusters, discriminated from pure star formation by means of standard diagnostics, e.g. BPT (Baldwin et al. 1981) and EW α 2 (Cid Fernandes et al. 2010) diagrammes.

(3) The study of the distribution of galaxy metallicities with cluster radii is another powerful mean to investigate evolution within clusters. As galaxies fall into clusters and travel toward the cluster center along their radial orbits, they interact with the intra-cluster medium (ICM) and other cluster galaxies, thus getting progressively stripped of their gas reservoir. This process is expected to influence their metal abundances and possibly generate a metallicity gradient across a cluster. Not much is yet known on the metallicities of emission-line galaxies in clusters and how it varies with cluster-centric distances. GLACE will allow to derive extinction-corrected metallicities using N2 (Denicoló et al. 2002), R23 (Pagel et al. 1979), and O3N2 (Alloin et al. 1979), where N2 and O3N2 will be used to break the R23 degeneracy and to assess possible differences between N and O abundances vs metallicity.

The survey addresses many other interesting topics: for instance the cluster accretion history can be traced by studying the census of ELGs at different cluster-centric distances. In addition, the survey will provide an accurate assessment of cluster membership, without the need of a spectroscopic follow-up.

2.2. GLACE implementation and TF principles

Regarding the technical implementation, the GLACE survey exploits the outstanding characteristics of the tunable filters (TF; González et al. 2014; Cepa et al. 2005, 2003); these are special Fabry-Perot interferometers in which the two plane parallel transparent plates (covered with high-reflectivity, low-

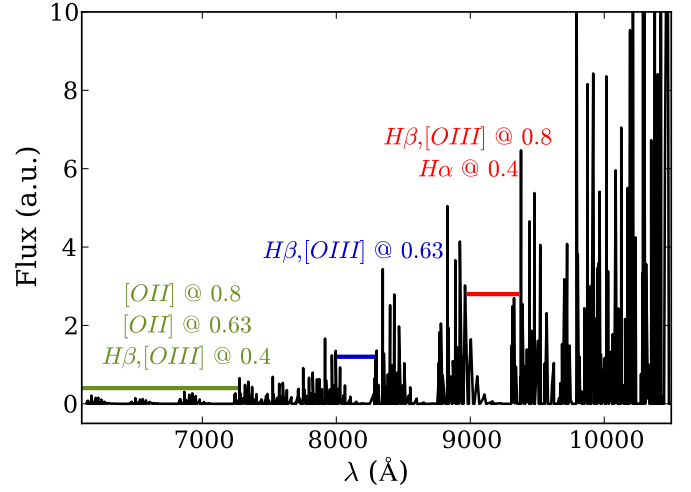


Fig. 1. Night sky spectrum from Rousselot et al. (2000) and GLACE windows within the OH bands. The loci of the strongest rest-frame emission lines at different redshifts are shown next to the corresponding spectral windows. The observations within this paper have been performed within the H α window at $z = 0.4$.

absorption coatings) are operated at much smaller spacing than the traditional ones (typically few microns). Hence, a broadened central interference region is produced (known as the Jacquinot spot, defined as the region over which the change in wavelength does not exceed by $\sqrt{2}$ times the FWHM). Moreover, controlled by means of a stack of piezo-electric transducers, the plate spacing can be varied with high accuracy over a large range. Therefore, a wide spectral region is accessible with a moderate spectral resolution (of the order of 10–20 Å FWHM): in the case of the OSIRIS red TF, the spectral range is 6510–9345 Å.

The TF transmission profile (Airy function) is periodic with the incident light wavelength. For a beam entering the TF at incidence angle θ , the condition for a maximum transmission (constructive interference) is:

$$m\lambda = 2\mu d \cos \theta \quad (1)$$

where m is the integer order of interference, μ is the refractive index of the medium in the cavity between the plates (usually air, $\mu = 1$) and d is the plate separation (gap). In order to select just one wavelength and order, additional intermediate-band filters, known as order sorters, are required. Since light coming from targets at increasing distance from the OSIRIS optical centre reaches the TF at increasing incidence angle, there is a progressive shift towards the blue as the distance r of the source to the optical centre increases. For the OSIRIS red TF, the dependency of the transmitted wavelength on the radial distance is given by González et al. (2014):

$$\lambda = \lambda_0 - 5.04r^2 + a_3(\lambda)r^3 \quad (2)$$

where λ_0 is the central wavelength tune in Å, r is the distance to the optical centre in arcmin and $a_3(\lambda)$ is an additional term expressing the wavelength dependency of the coatings, given by:

$$a_3(\lambda) = 6.0396 - 1.5698 \times 10^{-3}\lambda + 1.0024 \times 10^{-7}\lambda^2 \quad (3)$$

Within a wavelength period, the TF transmission profile $T(\lambda)$ can be approximated by the expression:

$$T(\lambda) \approx \left(1 + \left(\frac{2(\lambda - \lambda_0)}{\Delta_{FWHM}} \right)^2 \right)^{-1} \quad (4)$$

where λ_0 is the wavelength at which the TF is tuned and Δ_{FWHM} is the TF FWHM bandwidth.

Within the GLACE survey, we have applied the technique of TF tomography (Jones & Bland-Hawthorn 2001; Cepa et al. 2013): for each line, a set of images are taken through the OSIRIS TF, each image tuned at a different wavelength (equally spaced), so that a rest frame velocity range of several thousands km/s (6500 km/s for our first target) centred at the mean cluster redshift is scanned for the full TF field of view of 8 arcmin in diameter. Additional images are taken to compensate for the blueshift of the wavelength from centre to the edge of the field of view (as given in Eq. 2). Finally, for each pointing and wavelength tuned, three dithered exposures allow correcting for etalon diametric ghosts, using combining sigma clipping algorithms.

The TF FWHM and sampling (i.e.: the wavelength interval between consecutive exposures) at H α are of 12 and 6 Å, respectively, to allow deblending H α from [N II] λ 6584, with an accuracy better than 20% (Lara-López et al. 2010). For the rest of the lines, the largest available TF FWHM, 20 Å is applied, with sampling interval of 10 Å. These parameters also allow a photometric accuracy better than 20% according to simulations performed within the OSIRIS team. The same pointing positions are observed at every emission line. In order to trace the relation between SF and environment in a wide range of local densities, We have required to cover ≈ 2 Virial radii (some 4 Mpc) within the targeted clusters. This determines the number of OSIRIS pointings (two pointings at 0.40 and 0.63 and just one at 0.86).

The intended GLACE sample includes nine clusters, three in each redshift bin. Currently we have been awarded with observing time and completed the observations of clusters: ZwCl 0024.0+1652 and RX J1257.2+4738. Tab. 1 outlines the sample and the current status of the observations.

3. Observations and data reduction

Two OSIRIS/GTC pointings using the red TF were planned an executed towards Cl0024. The first one (carried out in GTC semesters 09B, 10A and 13B; hereafter referred as “centre position”) targeted the H α /[N II], H β and [O III] lines. The observations were planned to keep the cluster core well centered within CCD1². The second pointing (hereafter referred as “offset position”) was carried out in semesters 10B and 13B and targeted the same emission lines. This second pointing was offset by $\Delta\alpha = -2.3$ arcmin, $\Delta\delta = +2.5$ arcmin (i.e. some 3.4 arcmin in the NW direction). A summary of the observations is presented in Tab. 2. Within the scope of this paper, we shall present the results from the H α /[N II] observations. The total on-source exposure time is 5.1 and 2.9 hours at the central and offset pointings, respectively.

The H α /[N II] spectral range 9047–9341 Å was covered by 50 evenly spaced scan steps³ ($\Delta\lambda = 6$ Å). Taking into account the radial wavelength shift described by Eq. 2, the spectral range sampled over the entire field of view (of 8 arcmin diameter) is somewhat smaller, 9047–9267 Å (the ranges 9267–9341 Å and 8968–9047 Å are partially covered in the central and external regions of the field of view, respectively). At each TF tune, three

individual exposures with an “L” shaped dithering pattern of 10 arcsec amplitude were taken (in order to allow the removal of fringes and to ease the identification of diametric ghosts; the amplitude was chosen similar to the gap between the detectors). While this observing strategy has revealed useful for removing the fringing patterns that are specially evident beyond $\lambda \approx 9300$ Å, it introduces an additional complexity since the position of a source within the CCD varies in each dither position, and therefore, the wavelength at which it is observed due to the radial wavelength shift experienced in TFs.

3.1. TF data reduction procedures

The data reduction was performed using a version of the `TFRED` package Jones et al. (2002) modified for OSIRIS by A. Bongiovanni (Ramón-Pérez et al. in prep.) and private `IRAF`⁴ and `IDL` scripts written by our team. The basic reduction steps were carried out using standard `IRAF` procedures and included bias subtraction and flat-field normalization; the next reduction step was a TF-specific one, namely the removal of the diffuse, optical-axis centred sky rings produced by atmospheric OH emission lines as a consequence of the radial-dependent wavelength shift described by Eqs. 2 and 3; to this end, the `TFRED` task `tringSub2` was used. It corrects each individual exposure by means of a background map created by computing the median of several dithered copies of the object-masked image. Fringing was also removed when required using the dithered images taken with the same TF tune. Then, the frames were aligned and a deep image obtained by combining all individual exposures of every scan step. This combination was done by applying a median filter. While this could potentially lead to the loss of line emitters with very low-continuum level, it is the best method to remove spurious features as ghosts. When compared with the deep image obtained adding up all the individual scans, applying a simple minimum-maximum rejection filter, we have observed that, at most, one line emitter per CCD gets lost but more than one-hundred spurious features are effectively removed. The astrometry was performed in the resulting deep image, using `IRAF` standard tasks (`ccxymatch` and `ccmap`). The sky position of reference objects were gathered from the USNO B1.0 catalogue (Monet et al. 2003) in the centre position, while for the offset one we obtained better results using the 2MASS catalogue (Skrutskie et al. 2006); the achieved precision was in both cases equal or better than 0.3 arcsec r.m.s. (i.e. of the order of the binned pixel size). The deep images were used to extract the sources by means of the `SExtractor` package (Bertin & Arnouts 1996). The number of sources detected above 3σ are 931 and 925 in the centre and offset positions, respectively (after removing a number of clearly spurious sources appearing at the edges of the detectors). Since there is a quite large overlap between both positions, we found 374 common sources after matching both source catalogues using `TOPCAT` (Taylor 2005). These common sources were used as a test of the relative consistency of our astrometry: 245 sources (65%) were found within a match radius of 0.5 arcsec (i.e. consistent with the quoted accuracy), 88 (24%) within 0.75 arcsec and 15 (4%) within 1.0 arcsec radius. A number of sources (26 objects, i.e. 7%) were matched at larger radii (around 1.5 arcsec) but these sources were always found at the edges of the images, where the OSIRIS field suffers a larger distortion.

² The OSIRIS detector mosaic is composed of two 2048×4096 pixel CCDs abutted, with a plate scale of 0.125 arcsec/pixel. See Cepa et al. (2005) and the OSIRIS Users’ manual at <http://www.gtc.iac.es/instruments/osiris/media>

³ three scan steps, at 9317.4 and 9323.4 and 9341.4 Å were accidentally omitted in the observations of the offset positions; hence only 47 slices are available for that pointing.

⁴ `IRAF` is distributed by the National Optical Astronomy Observatory, which is operated by the Association of Universities for Research in Astronomy (AURA) under cooperative agreement with the National Science Foundation.

Table 1. GLACE sample and status of the observations

Name	RA(J2000)	Dec(J2000)	z	Status
ZwCl 0024.0+1652	00 26 35.7	+17 09 45	0.395	Completed; programmes GTC63-09B, GTC8-10AGOS, GTC47-10B & GTC75-13B
Abell 851	09 42 56.6	+46 59 22	0.407	Planned
RX J1416.4+4446	14 16 28.7	+44 46 41	0.40	Planned
XMM1SS-XLSSC 001	02 24 57.1	-03 48 58	0.613	Planned
MACS J0744.8+3927	07 44 51.8	+39 27 33	0.68	Planned
Cl J1227.9-1138	12 27 58.9	-11 35 13	0.636	Planned
XLSSC03	02 27 38.2	-03 17 57.0	0.839	Planned
RX J1257.2+4738	12 57 12.2	+47 38 07	0.866	Completed; ESO/GTC programme 186.A-2012
Cl 1604+4304	16 04 23.7	+43 04 51.9	0.89	Planned; Cl 1604 supercluster

Table 2. Log of the OSIRIS/TF observations of the region centred around the H α emission line in the Cl0024 cluster.

Centre Position						
$\lambda_{0,i}$ (nm)	OS Filter	Date	Seeing (")	N Steps	N Exp.	Exp. Time (s)
904.74	f893/50	2009 Dec 05	0.7–0.9	6	3	53
		2010 Aug 17	0.8	6	3	85
908.34	f902/40	2010 Aug 21	0.8	11	3	60
908.74	f902/40	2009 Dec 05	0.7–0.9	2	3	53
909.54	f902/40	2009 Nov 25	0.9–1.1	9	3	53
914.94	f910/40	2009 Nov 25	0.9–1.1	9	3	53
		2010 Aug 01	0.8	14	3	60
920.34	f910/40	2009 Dec 05	0.6–0.8	5	3	53
923.34	f919/41	2009 Dec 05	0.6–0.8	4	3	53
		2010 Aug 18	0.8	3	3	60
925.14	f919/41	2010 Aug 18	0.8	5	3	100
928.14	f919/41	2010 Aug 18	0.8	3	3	120
929.94	f919/41	2010 Aug 19	0.9	3	3	190
931.74	f923/34	2010 Aug 19	0.9	2	3	170
932.94	f923/34	2010 Aug 21	0.8	3	3	120

Offset Position						
$\lambda_{0,i}$ (nm)	OS Filter	Date	Seeing (")	N Steps	N Exp.	Exp. Time (s)
904.74	f893/50	2010 Oct 01	<1.0	6	3	60
908.34	f902/40	2010 Nov 08	1.0–1.2	11	3	60
914.94	f910/40	2010 Sep 20	<0.8	14	3	60
923.34	f919/41	2010 Nov 08	0.9–1.2	3	3	60
925.14	f919/41	2010 Nov 08	0.9–1.2	5	3	100
928.14	f919/41	2010 Nov 08	0.9–1.2	3	3	120
929.94	f919/41	2010 Nov 08	1.0–1.2	3	3	120
932.94	f923/34	2010 Oct 01	<1.0	2	3	120

The catalogue of detections contains 1482 unique sources. For each detected source and scan step, the best possible combination of individual images, i.e. the best combinations of TF tune and dither position at the location of the source was computed. In practice, we deemed as “best combination” algorithm the selection of all the images for which the TF wavelength at the position of the source lies within a range of $\pm 3 \text{ \AA}$ (i.e. half scan step) of the given one. For each of these combinations, a synthetic equivalent filter transmission profile was derived by adding up the transmission profiles of all the images entering the combination and fitting to the result the function given in Eq. 4. These synthetic profiles allowed us to verify that our combination approach does not introduce a significant error neither in the wavelength of the central position (less than 1 \AA maximum) nor in the FWHM (the average equivalent FWHM is 12.7 \AA with a deviation of 0.4 \AA). The output combined image is used to determine the flux at this specific scan step and source position by means

of SExtractor. The resulting “pseudo-spectra” consist of 50 (47) tuples (λ at source position, flux). The FWHM of the equivalents (synthetic) TF Airy transmission profiles derived at each source position and TF tune were also included in each pseudo-spectrum file. A pseudo-spectrum should not be confused with a standard spectrum produced by a dispersive system: the flux at each point of the pseudo-spectrum is that integrated within a filter passband centred at the wavelength of the point; therefore, mathematically a pseudo-spectrum is the convolution of the source spectrum with the TF transmission profile.

3.2. Flux calibration

The flux calibration of each TF tune has been carried out in two steps: first, the total efficiency $\epsilon(\lambda)$ of the system (telescope, optics and detector) should be derived; it is computed as the ratio of the measured to published flux $F_m(\lambda)/F_p(\lambda)$ for a set of ex-

Table 3. Spectrophotometric standard stars

Name	m(λ)	Reference	Position
G157–34	15.35(5400)	Filippenko & Greenstein (1984)	offset
G191–B2B	11.9(5556)	Oke (1990)	offset
Ross 640	13.8(5556)	Oke (1974)	centre

Table 4. Efficiencies for Cl0024 observations

Position	$\lambda \leq 9270 \text{ \AA}$ $\langle \epsilon \rangle$	$\lambda > 9270 \text{ \AA}$ Zero point	Slope
Centre	0.1779 ± 0.0236	10.2497 ± 1.2181	-0.0011 ± 0.0001
Offset	0.1993 ± 0.0035	12.8566 ± 0.9074	-0.0014 ± 0.0001

posures of spectrophotometric standard stars (Tab. 3) taken in photometric conditions within a range of tunes compatible with that of the cluster observation (ideally at the same tunes). The fluxes of the standards are measured by aperture photometry, and the exact wavelengths at the positions of the star are derived from Eqs. 2 and 3. The published fluxes are also derived at these wavelengths by means of a polynomial fit to the tabulated fluxes (see references in Tab. 3). Then, measured fluxes in engineering units (ADU) are converted to physical units ($\text{ergs s}^{-1} \text{ cm}^{-2} \text{ \AA}^{-1}$) using the expression:

$$F_m(\lambda) = \frac{g K(\lambda) E_\gamma(\lambda)}{t A_{tel} \delta \lambda_e} F_{ADU}(\lambda) \quad (5)$$

where g is the CCD gain in $\text{e}^- \text{ADU}^{-1}$, $E_\gamma(\lambda)$ is the energy of a photon in ergs, t is the exposure time in seconds, A_{tel} is the area of the telescope primary mirror in cm^2 , $\delta \lambda_e$ is the effective passband width⁵ in \AA , and $K(\lambda)$ is the correction for atmospheric extinction,

$$K(\lambda) = 10^{0.4 k(\lambda) \langle \chi \rangle} \quad (6)$$

dependent on the extinction coefficient $k(\lambda)$ and the mean air-mass $\langle \chi \rangle$ of the observations. In our case, we estimated $k(\lambda)$ by fitting the extinction curve of La Palma⁶, in the wavelength range of interest.

The uncertainty in the efficiency has been computed by error propagation, taking into account the errors in the measured fluxes (that in turn include terms to cope with the error of the aperture photometry and the uncertainty of the wavelength tune) and those of the published ones.

The efficiency $\epsilon(\lambda)$ (sampled with 9 tunes at position A and 19 tunes at position B) must be then fitted to an analytical function of λ in order to perform the calibration at the wavelength of each tune and source. In both cases, the best solution has been a constant efficiency for $\lambda \leq 9270 \text{ \AA}$ and a linear decreasing dependency at longer wavelengths (Tab. 4).

The second step is to convert the measured flux in ADU of each source at each tune i to physical units ($\text{ergs s}^{-1} \text{ cm}^{-2} \text{ \AA}^{-1}$) by means of the expression:

$$f(\lambda)_i = \frac{g K(\lambda) E_\gamma(\lambda)}{t A_{tel} \delta \lambda_e \epsilon(\lambda)} f_{ADU,i} \quad (7)$$

where $\epsilon(\lambda)$ is the total efficiency computed above and the remaining terms are as in Eq. 5. The flux errors are computed again

by propagation, taking into account the efficiency errors derived above and the source flux measurement uncertainty computed by the `TFRED tspect` task as:

$$\Delta f = \sqrt{A_{pix} \sigma^2 + f/g} \quad (8)$$

where A_{pix} is the measurement aperture area in pixels, σ is the standard deviation of the background noise and g is the gain in $\text{e}^- \text{ADU}^{-1}$.

3.3. Ancillary data

Within the process of generation of the catalogue of line emitters and further data analysis, we have made use of public Cl0024 catalogues⁷ from the collaboration “A Wide Field Survey of Two $z=0.5$ Galaxy Clusters” (Treu et al. 2003; Moran et al. 2005, hereafter M05) that include photometric data for 73318 sources detected and extracted in the *HST* WFPC2 sparse mosaic covering 0.5×0.5 degrees (Treu et al. 2003) and in ground-based CFHT CFH12k *BVR* and Palomar WIRC *JK_s* imaging. Visually determined morphological types are given for all sources brighter than $I=22.5$. In addition, thousands of photometric and spectroscopic redshift estimates are available. The catalogue of spectroscopically confirmed objects within the field (including foreground, cluster and background sources) comprises 1632 sources (see Moran et al. 2007, and references therein).

4. The Catalogue of ELGs

In order to produce a catalogue of ELGs we start by selecting the line emitters. The first step to get the catalogue of ELGs is to perform the selection of line emitters (either H α at the redshift of the cluster, or other lines in the case of background contaminants). In many cases, the emission line showed very clear, and even in a fraction of the emitters the H α and [N II] lines appeared clearly resolved, but given the number of input sources, an automated or semi-automated procedure was required. The `TFRED` package provides with a task, `tscale`, that outputs the putative ELGs from the source catalogue, but when applied to our input catalogue, it did not yield reliable results: it was designed for a reduced number of scans and sparse spectral sampling and frequently failed to classify even the most obvious ELGs from our densely sampled pseudo-spectra. Instead, we have followed a different approach, creating an automatic selection tool, implementing the following steps: (i) Define a “pseudo-continuum” (hereafter referred as pseudoc) as the subset of pseudo-spectrum points resulting from discarding “high/low” outlier values, defined as those above/below the median value $\widetilde{flux}_{alldata} \pm 2 \times \sigma_{alldata}$; the “pseudo-continuum” level, $flux_{pseudoc}$, will be defined as its median and the “pseudo-continuum” noise, $\sigma_{pseudoc}$, as its standard deviation. (ii) The “upper” value will be defined as $flux_{pseudoc} + 2 \times \sigma_{pseudoc}$. Then, the criteria to determine a reliable ELG candidate have been defined as: A) either two consecutive values above “upper” are found, or B) or one point above “upper” is found and, in addition, one contiguous point above $flux_{pseudoc} + \sigma_{pseudoc}$ and one contiguous point above $flux_{pseudoc}$. These criteria have been chosen since we have observed in our simulations (see below) that even very narrow lines (0.7 \AA) always produce a high positive signal in at least two scan slices around the maximum. Single-point

⁵ $\delta \lambda_e = \frac{\pi}{2} FWHM_{TF}$
⁶ <http://www.ing.iac.es/Astronomy/observing/manuals/ps/tech.notes/tn031.pdf>
⁷ <http://www.astro.caltech.edu/~smm/clusters/>

peaks in the pseudo-spectrum are attributed to noise or artefacts. On the other hand, the criteria above can cope with broad-line AGNs (see sect. 8).

In order to investigate the reliability of this automatic classifier, we have created a number of simulated spectra comprising an emission line with a Gaussian profile and a flat continuum (a good approximation within our relatively small spectral range). This simple spectrum is convolved with an Airy profile with $\text{FWHM} = 12 \text{ \AA}$ and sampled at steps of 6 \AA to produce a noiseless pseudo-spectrum. Finally, a noise component is built drawing random values from a normal distribution with zero mean and varying standard deviation and added to the pseudo-spectrum signal. We have built a collection of 800 such pseudo-spectra varying different input parameters, namely: (i) the range of intrinsic line widths of the lines has been adopted from the typical limiting values of the integrated line profiles of giant extragalactic HII regions from Roy et al. (1986), from some 20 km s^{-1} to about 40 km s^{-1} that corresponds to a range $\text{FWHM}_{\text{line}} = 0.7\text{--}1.5 \text{ \AA}$ (rest frame) with 0.4 \AA step; this range has been further extended by one additional step up to 2.3 \AA (65 km s^{-1}) in order to cope with blending of several HII regions within the galaxy; (ii) the range of shifts of the peak of the line with respect to the maximum filter transmission has been set to $0\text{--}3 \text{ \AA}$ with 1 \AA step (i.e. consistent with the scan step of 6 \AA); (iii) the equivalent width (EW) of the emission line has been varied in the range $5\text{--}15 \text{ \AA}$ with steps of 1 \AA (this range explores our detection sensitivity threshold; at larger EW we do not expect line identification problems) (iv) and finally, the amplitude (standard deviation) of the added random noise component, σ_{noise} , has been set in the range 0.1 to 0.4 times the maximum of the line, with steps of 0.1.

The automatic classifier has identified as line emitters 726 out of the 800 simulated pseudo-spectra (i.e. more than 90%). From those, only in two cases the classifier chose the source based in a noise feature rather than the correct line. As expected, the 74 pseudo-spectra not classified as ELG are in the high noise range (0.3 or 0.4).

Moreover, in order to determine the possibility of automatically classifying as ELG a passive galaxy, we have generated in a similar way a set of pseudo-spectra based on a flat continuum and σ_{noise} in the range 0.1 to 0.3 times the continuum flux value, with steps of 0.01 (a finer step was chosen in order to create a sufficient large number of instances, given that the noise is the only variable parameter). At each noise step, we have generated 21 instances yielding a total number of 420 pseudo-spectra. From these, 316 (i.e. more than 75%) have been classified as passive, while the remaining 104 (i.e. less than 25%) have been classified as ELG.

The results of the simulations indicate that our simple classification algorithm is quite effective to classify true ELGs as a line emitters, but can also pick a non-negligible amount of noisy pseudo-spectra of passive galaxies as emission-line objects. Therefore, we have added an additional step, filtering the sample produced by the selection tool by a careful visual inspection of the pseudo-spectra and also of the thumbnails of all scan slices for every source of this output sample (this was done by three collaborators separately). After applying these two steps, we have extracted a sample of 210 very robust (i.e. high S/N) ELGs, comprising both star-forming galaxies and AGNs.

4.1. Line wavelength estimation

Estimating the wavelength of the $H\alpha$ line is possible with TF tomography, but it is generally a complex issue, since on the one hand, we have a blend of three lines (the $H\alpha$ line plus the two components of the $[\text{NII}]$ doublet), convolved with the transmission profile of the TF and, as will be described in sect. 5, in many cases the pseudo-spectrum line “profile” (hereafter referred as line pseudo-profile) is affected by absorption-like features. We have attempted to derive the $H\alpha$ line position considering a model comprising three Gaussian lines plus a linear continuum; the rest-frame wavelength relative positions are fixed, as is the ratio of the two $[\text{NII}]$ doublet components (set to $f_{6548}/f_{6583} = 0.3$). Free parameters of the model are: the observed wavelength of the $H\alpha$ line, the line width (constrained to be the same for the three lines), the $[\text{NII}] \lambda 6583$ and $H\alpha$ fluxes and the continuum level. This model spectrum has been convolved with the TF transmission profile and fitted by means of non-linear least squares to the pseudo-spectra profiles. For some 30% of the sources, the result of the fit reproduces accurately the pseudo-spectrum profile, but in a vast majority of the cases the fit either fails or provides inaccurate results due to noise in the pseudo-continuum, absorption-like features in the line pseudo-profile, etc. Eventually, we have decided to derive the position of the line by manually fitting the pseudo-spectrum using the IRAF `splot` task and either a Gaussian or a Lorentzian profile, choosing after inspection the appropriate range to avoid continuum noise and contaminant lines. There is a very good agreement between the line positions computed by `splot` and those resulting from the trustful, accurate model fits ($\sim 1 \text{ \AA}$). In a minority of the cases, where the line profile showed very asymmetric (e.g. when absorption-like features are present, most likely due to random noise as shown in sect. 5 below), the position of the line was chosen to be the peak value of the pseudo-spectrum. Given the difficulty of providing a trustful uncertainty figure, we have assumed a constant error value of 3 \AA for the fit to the peak of the line, i.e. half of a scan step; this error is square-added to the tuning uncertainty of 1 \AA and to the wavelength error introduced by the combination of images performed in order to produce the pseudo-spectrum (see sect. 3.1), also considered to be 1 \AA at most; hence, $\sigma_{\text{pos}} \simeq 3.3 \text{ \AA}$.

4.2. Identification of $H\alpha$ emitters: rejection of interlopers

The observations presented here target a single emission line; therefore, a number of interlopers can be present; these are expected to be ELGs at other redshifts. When observing $H\alpha$ at $z = 0.40$, $[\text{OIII}] \lambda 5007 \text{ \AA}$ emitters at $z = 0.83$ and $[\text{OII}] \lambda 3727 \text{ \AA}$ emitters at $z = 1.46$ can be detected as well. However, at the limiting fluxes considered here these contaminants are not expected to be very abundant and can be easily discriminated via colour-colour diagrams. We have implemented such colour-colour diagnostic diagrams following Kodama et al. (2004) according to the following steps: first, we have matched our initial catalogue of 210 robust candidates with the photometric and spectroscopic catalogue from M05 and a matching radius of 1.0 arcsec (i.e. compatible with the accuracy of our astrometry). A counterpart with at least photometric data has been found for 202 sources. Using the CFHT CFH12k aperture photometry, we have computed the $B - V$, $V - R$ and $R - I$ colours. The diagnose grid has been built by deriving synthetic colours for COSMOS templates Ilbert et al. (2009) of Sa, Sc, and starburst (SB) galaxies at redshifts ranging from $z = 0$ to $z = 1.0$ with steps of 0.1, in-

tegrated to the CFH12k B , V , R and I passbands. Also, models from Kodama et al. (1999) at $z=0.4$ and $z=0.5$ have been included in the grid. The diagrammes for $B-V$ vs. $V-R$ and $V-R$ vs. $R-I$ are shown in Fig. 2. A source has been deemed as interloper if: (i) the source is outside the cluster region (as depicted in Fig. 2) in both colour diagrammes and does not have a spectroscopic redshift from M05 within the cluster range (set as $0.35 \leq z \leq 0.45$); (ii) the source has a spectroscopic redshift from M05 outside the cluster range, independent of its colours.

Based on the first criterion, we have deemed 19 sources as contaminants. These are in a vast majority of the cases located in the locus of the colour-colour diagram occupied by galaxies at $z=0.8-1.0$, i.e. consistent with being $[O III]\lambda 5007 \text{ \AA}$ emitters. Moreover, 97% of the ELGs with a redshift from M05 within the cluster range have been also catalogued as cluster members by the colour-colour diagnostic described above. The second criterion added 9 additional sources as interlopers (two sources have been discarded by both colours and redshift criteria). Hence, 28 objects have been classified as contaminants at a different redshift. In addition, 8 sources do not have a counterpart in the M05 catalogue and therefore have been excluded from the cluster list. Therefore, our final catalogue consists of 174 robust cluster $H\alpha$ emitters (see the distribution of sources in the sky in Fig. 4), 28 putative interlopers (ELGs at a different redshift, mostly oxygen emitters at $z \sim 0.9$) and 8 sources without ancillary data to perform the assessment. Future analysis of additional spectral ranges (centred at the $[O III]$ and $H\beta$ wavelengths at the nominal redshift of Cl0024) will refine this rejection criterion. The 174 sources in our final catalogue of unique robust cluster emitters are listed in Tab. 5. From these, 112 have spectroscopic redshifts in the M05 catalogue.

Fig. 3 shows a selection of high signal-to-noise pseudo-spectra. In many cases, the strongest $[N II]$ doublet component (at 6583 \AA) is clearly separated from the $H\alpha$ line in a visual inspection. Sometimes the line is observed as a “shoulder” at the long wavelength side of the $H\alpha$ line.

5. Derivation of line fluxes

From the pseudo-spectra described in sect. 4, it is possible to derive the $H\alpha$ and $[N II]$ fluxes following several approaches. We have applied a straightforward procedure derived from the standard narrow-band on-band/off-band technique, using for each source the flux in the scan slice closest to the computed position of the $H\alpha$ line (see sect. 4) and that of the slice closest to the $[N II]$ line; as will be shown below, this method, though simple, produces acceptable results when compared to the more sophisticated procedure based on least-squares fitting of the pseudo-spectrum to a model spectrum convolved with the transmission profile of the TF described in sect. 4.1 with the advantage that the former method is always applicable while the latter can be only used in a minority of cases.

We start by subtracting a linear continuum. This can be easily done by applying a linear fit to the regions of the pseudo-spectrum excluding the emission line. Then, assuming infinitely thin lines, the $H\alpha$ and $[N II]$ line fluxes, denoted by $f(H\alpha)$ and $f([N II])$ respectively, are given by the expressions (Cepa, priv. comm.):

$$\begin{aligned} f_{on,H\alpha} &= T_{H\alpha}(H\alpha) f(H\alpha) + T_{H\alpha}([N II]) f([N II]) \\ f_{on,[N II]} &= T_{[N II]}(H\alpha) f(H\alpha) + T_{[N II]}([N II]) f([N II]) \end{aligned} \quad (9)$$

where $f_{on,H\alpha}$ and $f_{on,[N II]}$ are the continuum-subtracted fluxes in the chosen $H\alpha$ and $[N II]$ slices and $T_{<slice>}$ ($< line >$) denotes the TF transmission of a given slice at a given line wavelength. The different transmission values can be easily derived from the approximate expression given in Eq. 4. From Eq. 9 we can easily derive the flux in the $H\alpha$ line:

$$f(H\alpha) = \frac{f_{on,H\alpha} T_{[N II]}([N II]) - f_{on,[N II]} T_{H\alpha}([N II])}{T_{H\alpha}(H\alpha) T_{[N II]}([N II]) - T_{H\alpha}([N II]) T_{[N II]}(H\alpha)} \quad (10)$$

And a similar expression for the $[N II]$ line. The errors in the lines have been derived by propagation, taking into account not only the errors in the $H\alpha$ and $[N II]$ “on” bands, but also the continuum noise (i.e. the noise around the zero-level continuum after removing the linear fit explained above). Hence, the line error has been computed as:

$$\begin{aligned} \Delta f(H\alpha) &= ((T_{[N II]}([N II]) \Delta f_{on,H\alpha})^2 \\ &+ (T_{H\alpha}([N II]) \Delta f_{on,[N II]})^2 \\ &+ ((T_{[N II]}([N II]) - T_{H\alpha}([N II])) \sigma_{cont})^2)^{1/2} \\ &/ (T_{H\alpha}(H\alpha) T_{[N II]}([N II]) - T_{H\alpha}([N II]) T_{[N II]}(H\alpha)) \end{aligned} \quad (11)$$

where $\Delta f_{on,H\alpha}$ and $\Delta f_{on,[N II]}$ are the flux errors in the “on” $H\alpha$ and $[N II]$ bands computed as indicated in sect. 3.2 and σ_{cont} is the continuum error measured as the standard deviation of the points within the region of the pseudo-spectrum excluding the emission lines. The contribution of the continuum noise to the total error is important, on average $\sim 30\%$ at the central position and much larger at the offset position where the exposure times are smaller, on average 60–70%.

The median fractional error in the $H\alpha$ fluxes is $\approx 24\%$. A 70% of the sample objects have relative errors below 30%. This errors are compatible with those quoted by Lara-López et al. (2010) (see sect. 2.2), though somewhat larger than those derived from their simulations due to our larger continuum errors. However, since the $[N II]$ line is usually fainter than the $H\alpha$ line, its flux errors are in general notably larger: the average fractional error is $\approx 54\%$ and only 15% of the sample objects have a relative error below 30%. This was of course expected since the detection/selection algorithm is driven by the strongest line present in the pseudo-spectrum. Hence, in many cases the $H\alpha$ line acts as a “prior” and the nitrogen flux is extracted at the expected wavelength of the (otherwise barely detected) $[N II]$ line.

As mentioned above, the line flux estimation is based in an infinitely thin line approximation which assumes that the line can be well represented by $\delta(\lambda - \lambda_z)$, where $\lambda_z = \lambda_0(1 + z)$. According to Pascual et al. (2007), for star-forming galaxies, emission line widths are mass-related and typically $\text{FWHM} \lesssim 10 \text{ \AA} \times (1 + z)$, and, for narrow-band filters of some 50 \AA width, it is possible to recover $\sim 80\%$ of the line flux up to $z \sim 4$. We have investigated the impact of applying such approximation to our very narrow TF scans ($\sim 12 \text{ \AA}$). To this end, we have performed several simulations using Gaussian line profiles of several widths peaking at different offsets with respect to the maximum of the filter transmission profile (Eq. 4). The emission line broadening is given by the relation (Fernández Lorenzo et al. 2009):

$$2V_{max} = \frac{\Delta\lambda c}{\lambda_0 \sin(i)(1 + z)} \quad (12)$$

where V_{max} is the maximum rotation velocity, λ_0 is the line wavelength at $z=0$ and $\Delta\lambda$ is the line width at 20% of peak

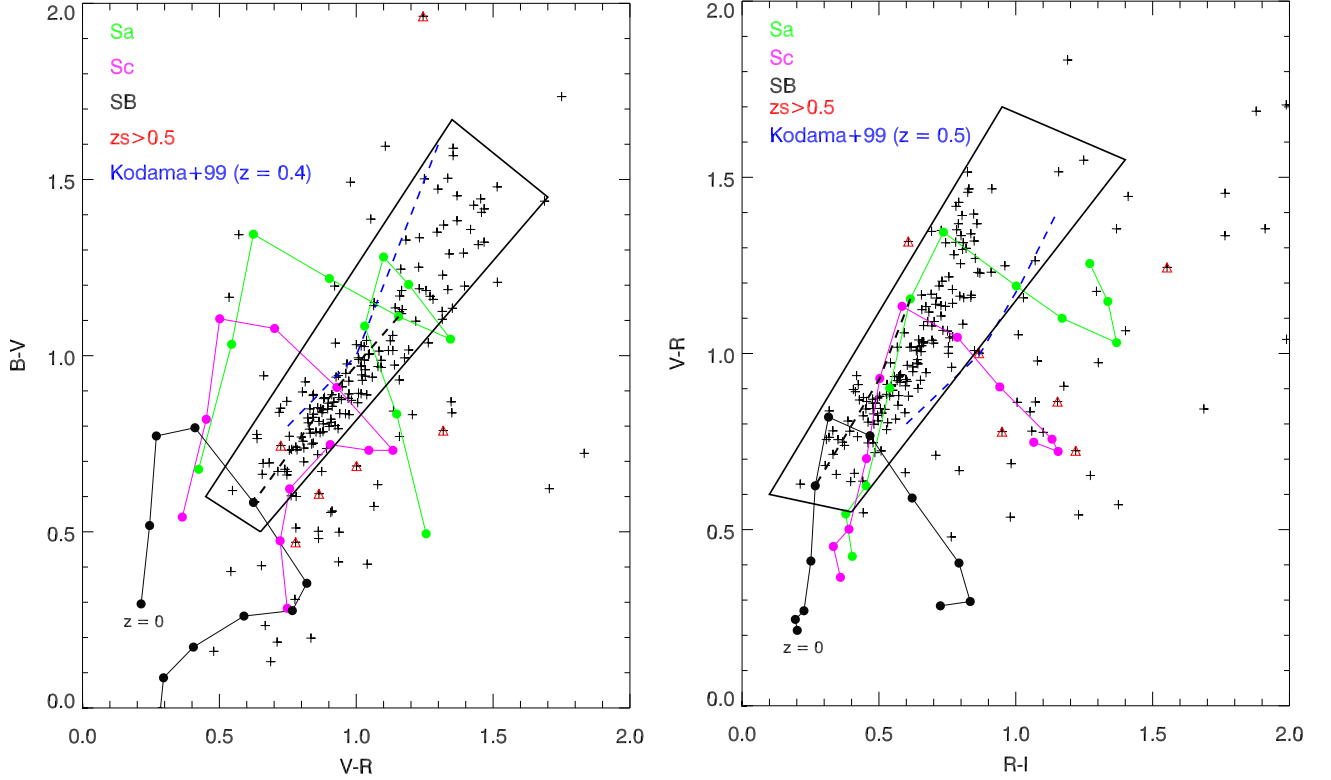


Fig. 2. $B - V$ vs. $V - R$ (left) and $V - R$ vs. $R - I$ (right) diagnostic diagrams. The sample, comprising 202 unique objects with counterparts in the M05 catalogue is denoted by cross symbols (+). The red triangles (Δ) mark objects with spectroscopic redshift $z_s > 0.5$ in the M05 catalogue. The control grid has been built using synthetic colours from COSMOS templates for Sa, Sc and SB galaxies in the range $z = 0.0-1.0$ with steps of $\Delta z = 0.1$. The thick, black dashed line connects the three templates at $z = 0.4$. The blue dashed line depicts the Kodama et al. (1999) models at $z = 0.4$ and $z = 0.5$. The thick, black solid line box marks the approximate region used for selecting the cluster candidates.

intensity. For a Gaussian line, $\Delta\lambda = 1.524 \times \text{FWHM}$. Assuming $V_{\max} = 200 \text{ km s}^{-1}$ as a safe upper limit (see for instance Fernández Lorenzo et al. 2009), the $H\alpha$ line $\text{FWHM} \approx 8 \text{ \AA}$ (here we assume that the line is unresolved. The possibility that the line appears resolved in our pseudo-spectra due to kinematical split is investigated below). For narrow lines, $\text{FWHM} = 2 \text{ \AA}$, we are able to recover 96–98% of the flux (from 0 to 2 \AA offset), while for the widest simulated lines, $\text{FWHM} = 8 \text{ \AA}$, the fraction of recovered flux is in the range 73–76%. In order to compare the simulations with real results, we have used the small set of pseudo-spectra for which a reliable fit to the model spectrum was achieved, finding that the average ratio between the flux derived from the infinitely thin line approximation and that derived from the best fit is 0.81 and 0.88 for the $H\alpha$ and $[\text{N II}]$ lines, respectively, i.e. well aligned with the results of our simulations.

The completeness limit of the ELG sample, as given by the maximum of the flux histogram depicted in Fig. 5 (left panel) is $\sim 0.9 \times 10^{-16} \text{ erg s}^{-1} \text{ cm}^{-2}$, i.e. better than the GLACE requirements.

5.1. Absorption-like features in the pseudo-spectra

In a large number of cases, we have observed in the pseudo-spectra absorption-like features affecting the (putative) $H\alpha$ emission line. This affects around 50% of the galaxies, and shows very clear in about 25% of the cases, as those depicted in Fig. 6. We have explored a number of possible explanations: first, and perhaps most obvious, that the absorption-like features are due

to random noise. These characteristics have been observed in the simulations described in the preceding sections, in approximately 20% of the cases (some 146 out of 726 simulated pseudo-spectra classified as ELGs). This is therefore a very probable explanation in an ample fraction of cases. In addition, we have explored two potential physical explanations: either an emission line split due to the galaxy rotation or the presence of underlying stellar absorption. In order to investigate the first possible cause, we have performed a series of simulations similar to those described in the preceding section but starting with a spectrum comprising two identical Gaussian lines with separation $2\lambda_0(1+z)V_{\max}/c$ and a flat continuum in order to re-create the effect of the rotational split in TF pseudo-spectra. We have built our collection of pseudo-spectra varying the range of intrinsic line widths in the range $\text{FWHM}_{\text{line}} = 0.7-2.3 \text{ \AA}$ (rest frame) with 0.4 \AA step; the range of shifts of the peak of the line with respect to the maximum filter transmission has been set to $0-3 \text{ \AA}$ with 1 \AA step and finally the galaxy rotational speed has been let to vary in the range $V_{\max} = 100-200 \text{ km s}^{-1}$ with 10 km s^{-1} step, in agreement with Fernández Lorenzo et al. (2009); hence, the separation between the two line peaks ranges from some 6.1 \AA to about 12.3 \AA ; and finally the amplitude of the added random noise component (σ_{noise}) has been set in the range 0.1 to 0.3 times the maximum of the line, with steps of 0.1.

After inspecting 1320 pseudo-spectra simulated as described above, we have observed that the fraction of absorption-like features observed in the pseudo-spectra is relatively low at rotational speeds $\leq 160 \text{ km s}^{-1}$, ranging from approximately 10% at

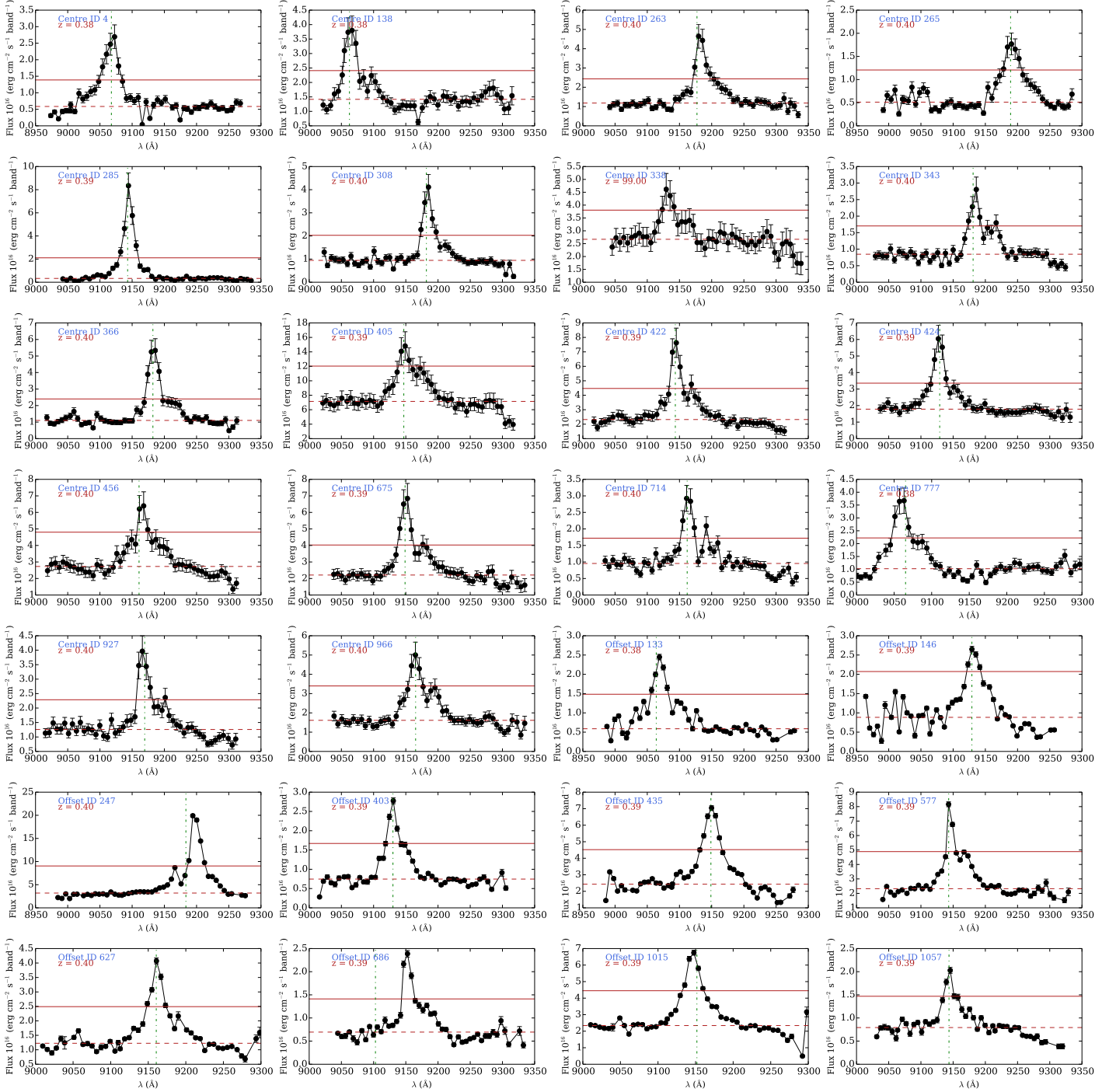


Fig. 3. Selection of 28 pseudo-spectra with high signal-to-noise. The green dashed-dotted lines correspond to spectroscopic or secure photometric redshifts from M05 (when available). The dashed red line corresponds to the approximate pseudo-spectrum continuum level, and the solid red line to the $3\sigma_{cont}$ level, where σ_{cont} is the pseudo-continuum noise. For the source ID offset/686, the redshift from M05 is photometric.

100 km s⁻¹ to some 26% at 160 km s⁻¹ and therefore consistent with noise-induced features. However, the fraction of features observed raises notably for $V_{max} \geq 170$ km s⁻¹, being of 45% at 170 km s⁻¹ and 58%–60% above that speed. Therefore, a kinematical line split due to galaxy rotation is a plausible mechanism to induce a fraction of the absorption-like features observed. Nevertheless, it should be taken into account that the fraction of such fast-rotating galaxies is reduced (around 14% in the sample of Fernández Lorenzo et al. 2009, in the range $0.3 < z < 0.8$) and

moreover that we are assuming $\sin i = 1$, i.e. edge-on or nearly edge-on galaxies so the actual fraction of objects fulfilling the conditions is probably on the order of 14% at most.

We have finally explored the possibility that these absorption-like features are caused by true absorption due to the underlying host galaxy stellar component. To this end, the most likely host galaxy stellar population was derived by fitting the public photometric information from M05 (B, V, R, I from CFHT; J, K_s from WIRC at Palomar 200”) by means

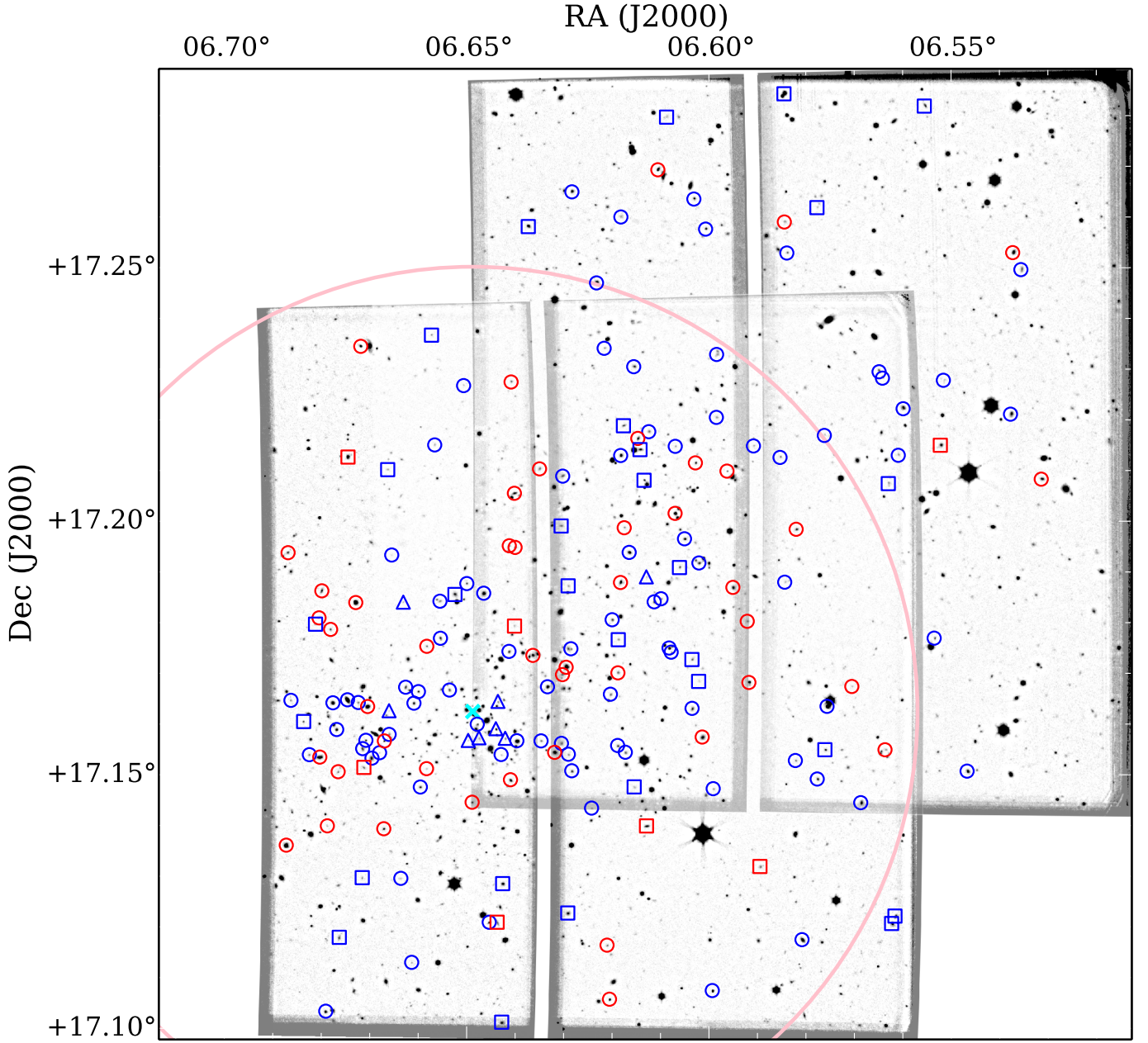


Fig. 4. The figure depicts the two OSIRIS/GTC pointings towards Cl0024. The plot has standard orientation: north is at the top and east to the left. Blue symbols correspond to SF galaxies and red ones correspond to AGNs according to the $[N II]/H\alpha \geq 0.6$ criterion from Ho et al. (1997). Circles correspond to galaxies in the main cluster structure (structure “A” in sect. 6), squares to those in the infalling group (structure “B”) and triangles to sources in the putative group around $z \approx 0.42$ (see sect. 6). The cyan cross (×) denotes the centre of the cluster (galaxies/BCG) and the large pink circle marks the virial radius of 1.7 Mpc (Treu et al. 2003). A general alignment of ELGs is observed in the NW–SE direction, consistent with a structure assembling onto the cluster core from the NW with an orientation almost in the plane of the sky (Moran et al. 2007; Zhang et al. 2005; Kneib et al. 2003).

of the *LePhare* code (Ilbert et al. 2006) using the set of SED templates from Bruzual & Charlot (2003), star formation histories exponentially declining with time as $SFR \propto e^{-t/\tau}$ with τ ranging from 0.1 to 30.0 Gyr, initial mass function (IMF) from Chabrier (2003) and dust extinction law from Calzetti et al. (2000). The details of the computations will be thoroughly described in Pérez-Martínez et al. (in prep.). The best-fitting host galaxy stellar template was furthermore re-sampled at a finer resolution using GALAXEV⁸ (Bruzual & Charlot 2003) and

then convolved with the TF transmission profile to obtain a “host galaxy stellar component” pseudo-spectrum. The pseudo-continuum of this synthetic pseudo-spectrum was then scaled to that of the real object within the range of the observations. In some cases, the absorption features were still present in the synthetic pseudo-spectrum and could account for at least a fraction of the absorption-like feature observed. However, due to the nature of the procedure, the best fit stellar template solution is notably degenerate when taking into account the photometric errors

⁸ <http://www2.iap.fr/users/charlot/bc2003/>

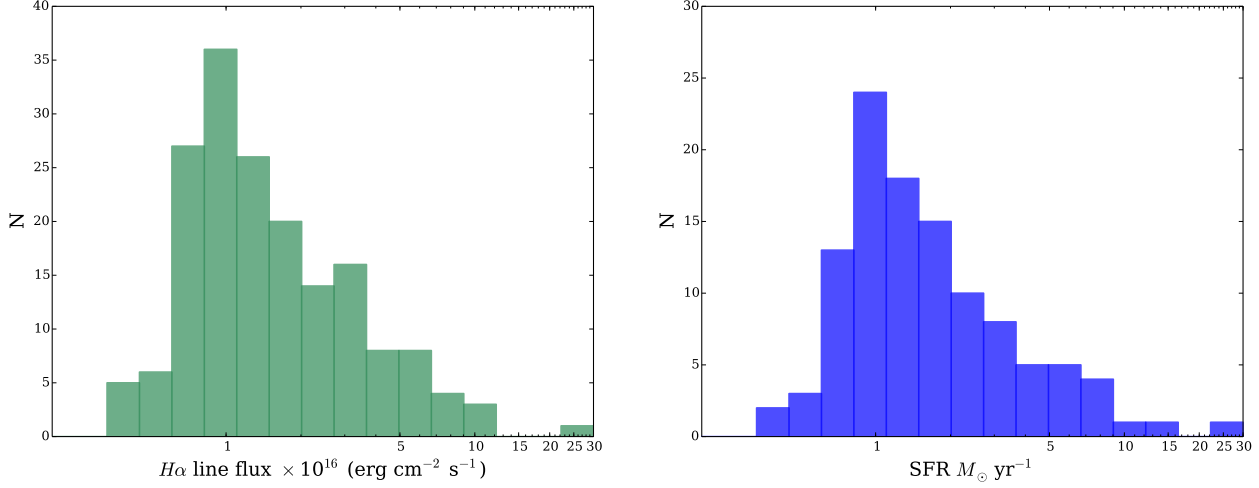


Fig. 5. *Left:* histogram of $H\alpha$ line fluxes for the 174 robust cluster members (after correcting for the strongest component of the $[N II]$ doublet). *Right:* histogram of SFR for SF galaxies (i.e. excluding AGN candidates) from the $H\alpha$ fluxes, applying a standard 1 mag. extinction correction for the line and the Kennicutt (1998) luminosity-SFR conversion.

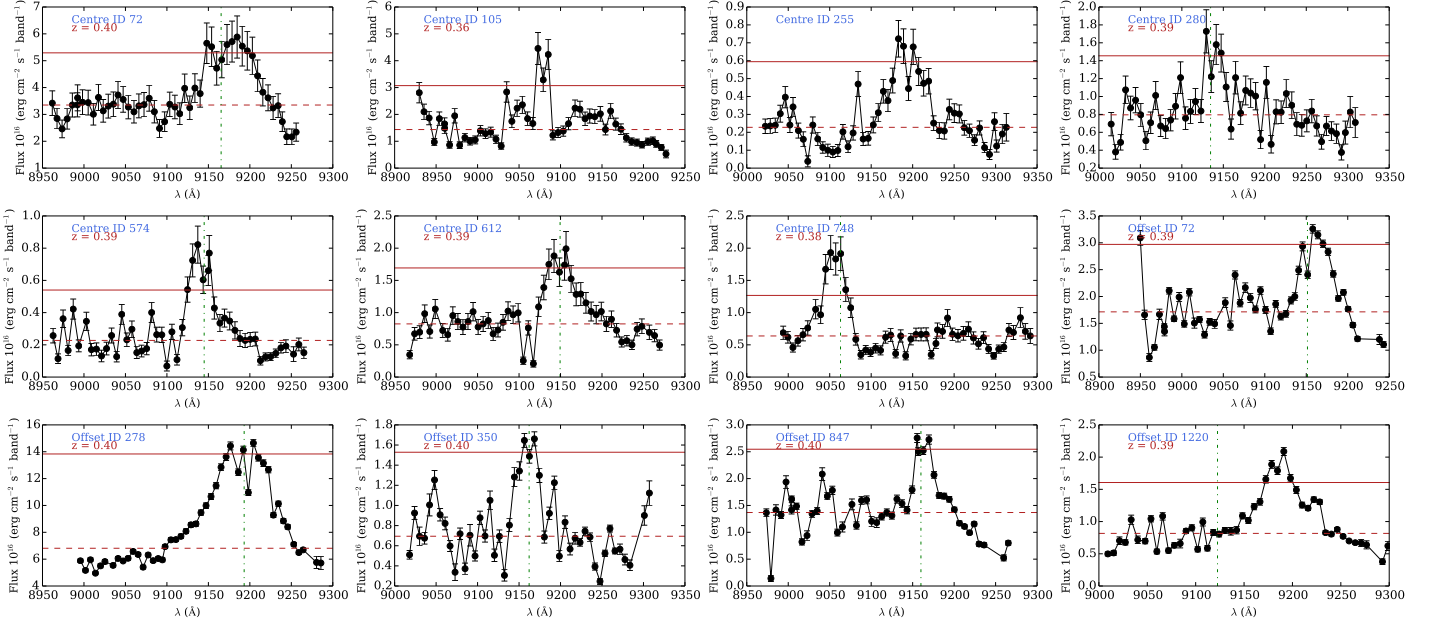


Fig. 6. Selection of pseudo-spectra with a variety of absorption-like features. Lines as in Fig. 3. For the source ID offset/1220, the redshift from M05 is photometric.

and therefore the flux correction is uncertain. Hence, we have decided to omit such correction for the $H\alpha/[N II]$ line fluxes.

6. Spatial and redshift distribution of the cluster galaxies

Spectroscopic redshifts from M05 were available for 112 of our ELGs (see sect. 4.2). In all cases, the M05 redshifts also placed our cluster candidates within the cluster. There was a remarkably good agreement between the redshift estimates derived from the position of the $H\alpha$ line within our pseudo-spectra (see line positions derived from spectroscopic redshifts in Fig. 3) and that derived from spectroscopic measurements. In fact, the redshift error defined as $|z_{TF} - z_{spec}|/(1 + z_{spec})$ is on average 0.002 (me-

dian value 0.0005) with a maximum value of 0.02, i.e. we can consider the TF-derived redshifts as of spectroscopic quality.

The spatial distribution of the ELG sample, as given by the position of the sources in the sky plane and our redshift estimates, maps the presence of two components: (i) a structure assembling onto the cluster core from the NW with an orientation almost in the plane of the sky. This structure has been already reported by other authors (Moran et al. 2007; Zhang et al. 2005; Kneib et al. 2003). (ii) An infalling group at high velocity nearly along the line of sight to the cluster centre, identified by a double-peaked distribution in the redshift space, as shown in Fig. 7 (Moran et al. 2007; Czoske et al. 2002): structure “A” (centred at $z = 0.395$) and “B” (centred at $z = 0.381$) correspond to the main cluster and infalling group components, respectively.

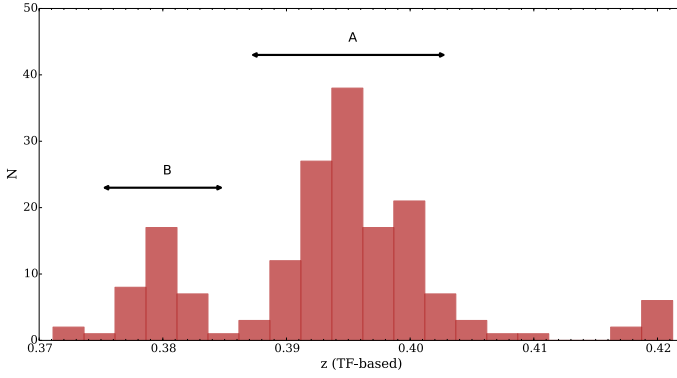


Fig. 7. Distribution of redshifts derived from our data. It is possible to recognize two dynamical structures as in Czoske et al. (2002): “A” is the main cluster component, while “B” lies along the line of sight to the cluster centre and has been interpreted as an infalling group at high velocity.

The distribution of galaxies can be also seen in Fig. 8, where the radial velocities relative to the central redshift of component “A” are plotted against the distance to the cluster centre as given by the distribution of galaxies/BGC (Treu et al. 2003). The two mentioned components are clearly separated. There is a third, small group of 8 galaxies at $z \approx 0.41$ – 0.42 (clearly seen in both Fig. 8 and Fig. 7) that has been also reported by Czoske et al. (2002). While according to these authors these galaxies are most likely part of the surrounding field galaxy population, we cannot rule out the possibility of another group connected to Cl0024. This suggestion could be reinforced by the fact that all these galaxies are observed within a relatively small cluster-centric projected distance, $r < 1$ Mpc. While this can be just a instrumental effect, result of the incomplete wavelength coverage at the red side of the velocity field, is should be taken into account that, on the one hand, the cluster centre is offset some 1 arcmin to the SE of the TF axis of the central pointing, and on the other, that no other excess of ELG is observed close to the TF axis of the offset pointing, as would be expected if the galaxies were part of the field galaxy population.

7. H α + [N II] luminosity function

In order to verify the accuracy and performance of our photometry, we have built the H α + [N II] luminosity functions computed from sources within a central area of 0.8 Mpc and within $r_{vir} = 1.7$ Mpc. These are depicted in Fig. 9. These cumulative functions can be compared with those of Kodama et al. (2004) (hereafter K04). However, while the comparison is direct at the smaller radius, at the larger one we need to take into account the fact that the coverage of our observations within r_{vir} is incomplete towards East and South-East, around 81% of the full circle of r_{vir} . We have performed a simple area correction to account for this, shown as a dotted-dashed line in the right panel of Fig. 9. The completeness of our sample, as measured by the peak of the luminosity histogram, is $\log L(H\alpha + [N II]) \approx 41$, very similar to that of K04.

An evident discrepancy between our data set and that of K04 is found at the high-luminosity end, $\log L(H\alpha + [N II]) \gtrsim 41.8$. This is observed, not only in the larger area but also in the smaller one, and hence it cannot be attributed to our incomplete area coverage. However, it should be taken into account that K04 results are based on different technique, namely a standard

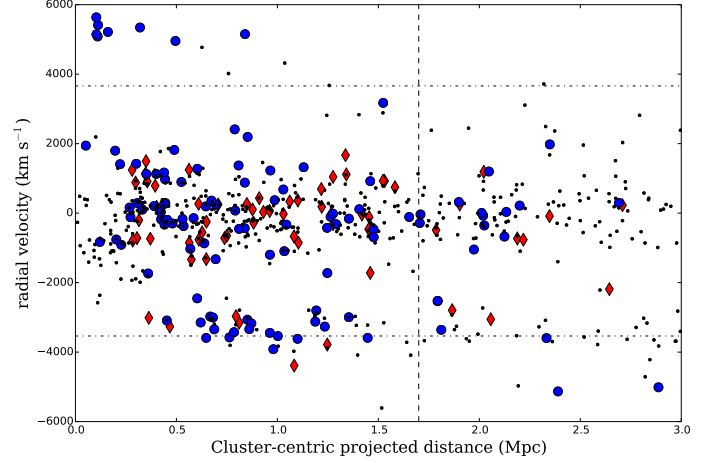


Fig. 8. Line-of-sight velocity relative to the cluster main component central redshift $z = 0.395$ plotted against the projected distance to the cluster centre (as defined by the distribution of galaxies/BGC). Red diamonds correspond to AGNs and blue dots to SF galaxies according to the H97 criterion (see sect. 8). The dotted vertical line marks the virial radius of 1.7 Mpc (Treu et al. 2003). The dashed-dotted horizontal lines correspond to the radial velocity limits fully covered within the field of view of both OSIRIS TF pointings (see sect. 3 and Eq. 2). The small, black points correspond to galaxies from M05 with spectroscopic redshifts, including both passive and star-forming objects.

narrow-band filter (the Subaru/Suprime-Cam NB₉₁₂ filter with $\lambda_{eff} = 9139$ Å and FWHM = 134 Å) plus broad-band BRz' filters and hence discrepancies in individual objects can be expected. Of course this affects only a few objects (just 4 objects down to $\log L(H\alpha + [N II]) \approx 41.8$). At lower luminosities and even beyond the completeness limit, the agreement between our cumulative number counts and those of K04 is excellent, reinforcing the confidence in the accuracy of our photometry.

8. Star-forming galaxies and the AGN population

We have explored the available mechanisms to separate the population of SF galaxies and AGNs. Broad-line AGNs (BLAGN) show permitted lines with widths of thousands of kilometers per second. By contrast, in narrow-line AGNs (NLAGN), spectra line Doppler widths are much smaller, typically only a few hundred kilometers per second, which is comparable to or somewhat larger than stellar velocity dispersions. We have verified that the profiles of broad lines are well reproduced in our data by simulating BLAGN pseudo-spectra built from real spectra of local universe Seyfert 1 (3C 120, García-Lorenzo et al. 2005) and Seyfert 1.5 galaxies (NGC 3516; Arribas et al. 1997), (NGC 4151; Kaspi et al. 1996), that were displaced to the redshift of Cl0024 and convolved with the TF transmission profile (Eq. 4). Finally, noise components built drawing random values from a normal distribution with zero mean and a standard deviation equal to 10% of the difference between the peak of the pseudo-spectrum and its median value were added to the pseudo-spectra signal. In all generated instances of such pseudo-spectra, the broad component of the H α line was clearly traced as depicted in Fig. 10.

In order to select candidates to BLAGN we have performed simple Gaussian fits to the pseudo-spectra, setting a low line

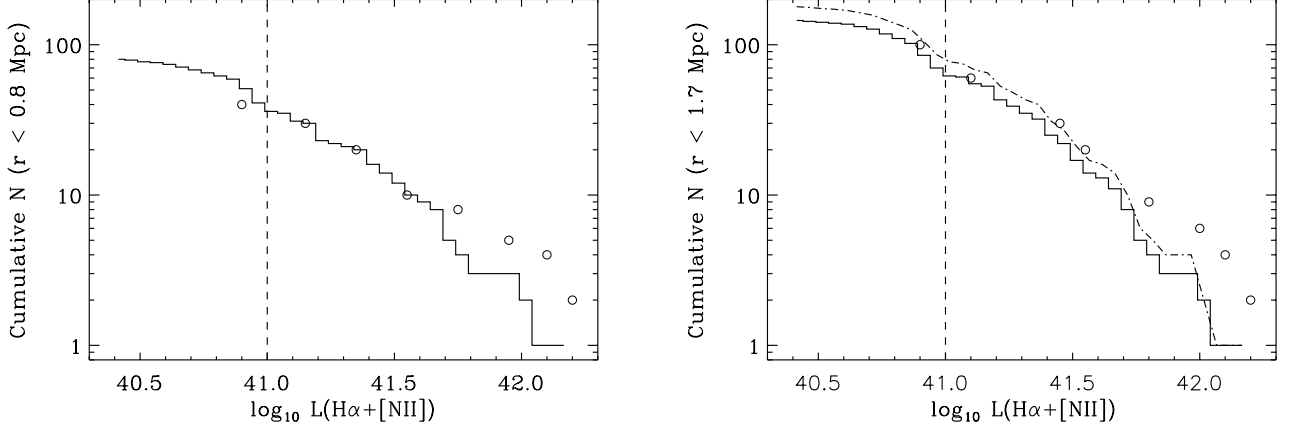


Fig. 9. Cumulative luminosity function (LF) within a radius of 0.8 Mpc (left) and $r_{vir} = 1.7$ Mpc (right). The solid line corresponds to our galaxy counts; the big open circles are sparsely sampled points from the Kodama et al. (2004) LF. The dotted-dashed line in the right plot corresponds to our LF corrected for the incomplete area coverage within r_{vir} . The dashed line corresponds to the completeness limit of our data, $\log L(H\alpha+[NII]) \simeq 41$.

width threshold of $FWHM = 36 \text{ \AA}$ (6 scan steps) that is approximately 1180 km s^{-1} at the redshift of Cl0024. The results of the fitting process were carefully inspected, rejecting incorrect or unclear cases (e.g. when two narrow lines were fitted as a single, broad one), arriving to a final list of 25 robust candidates, i.e. 14% of the sample of ELG. Some cases are depicted in Fig. 10.

In a second step, we have separated NLAGNs from SF galaxies using the ratio between the $[NII]$ and the $H\alpha$ lines. Moreover, following Cid Fernandes et al. (2010) we have combined this ratio with the equivalent width of $H\alpha$ ($W_{H\alpha}$) in order to break the degeneracy between Seyfert and LINER galaxies, the so-called ‘EW α n2 diagram’ as depicted in the left panel of Fig. 11. The use of $W_{H\alpha}$ is justified by the known fact that Seyfert galaxies tend to have a higher power of the ionising engine with respect to the optical output of the host stellar population. According to Cid Fernandes et al. (2010), a sensible Seyfert/LINER boundary can be set at $W_{H\alpha} = 6 \text{ \AA}$. On the other hand, the fraction of NLAGN depends on the limits set to $[NII]/H\alpha$. Different criteria have been proposed: Ho et al. (1997) (hereafter H97) adopted the classical criterion from Veilleux & Osterbrock (1987) and consider SF galaxies as those with $[NII]/H\alpha < 0.6$, and accordingly NLAGNs those in the region $[NII]/H\alpha \geq 0.6$. This region is populated by objects showing pure AGN spectral features (either Seyferts or LINERS) and ‘transition’ or ‘composite’ objects, interpreted as galaxies whose integrated spectra is the superposition of AGN and SF features. The criterion from Kewley et al. (2001) (K01) is widely used to separate ‘pure AGNs’ ($\log([NII]/H\alpha) \geq -0.10$) from SF and composite objects, while those of Kauffmann et al. (2003) (K03) and Stasińska et al. (2006) (S06) are used to separate ‘pure SF’ galaxies from any AGN or composite object. In Tab. 5 the fractions of NLAGNs found within our sample are shown after applying the different criteria explained above. Taking into account the fraction of BLAGNs found above, the total fraction of AGNs with respect to the ELG population ranges from 26% to 54% depending on the diagnostic used. Unless otherwise stated, the H97 criterion will be used hereafter to separate SF and NLAGN classes. According to this criterion, the fraction of BLAGNs with respect to NLAGNs is 64%, very similar to the fractions of Seyfert 1/Seyfert 2 in the local universe from

Ho et al. (1997, 61%) and Sorrentino et al. (2006, 60%) and the fraction (BLAGN+NLAGN)/ELG $\sim 37\%$.

Table 5. Fraction of NLAGNs in Cl0024 applying different criteria

Criterion	$[NII]/H\alpha$	NLAGN number	NLAGN Fraction (%)
‘pure AGN’ (K01)	≥ 0.794	21	12
‘Classical AGN’ (H97)	≥ 0.60	39	22
AGN+composite (K03)	≥ 0.478	60	34
AGN+composite (S06)	≥ 0.398	69	40

Regarding the AGN class, all the objects are very likely Seyfert galaxies ($W_{H\alpha} > 6 \text{ \AA}$). No clear LINER-class objects are detected due to our equivalent width detection limits.

A cautionary note regarding errors in our estimates: due to the large uncertainties quoted for the $[NII]$ line fluxes, the errors of the $[NII]/H\alpha$ ratios are also generally large; in fact, only 30% of the sample has relative errors below 50%, and these objects are in a vast majority AGNs and composite objects. Very large fractional errors in the $[NII]/H\alpha$ ratios tend to be found in objects where the $[NII]$ line is barely detected, and thus very likely pure SF galaxies. Hence we have eventually decided to keep all sources in the study, regardless of their error in the $[NII]/H\alpha$ ratio.

The fractions of AGNs with respect to the total number of ELGs obtained in this study are higher than our previous estimates for this cluster ($\sim 20\%$; Pérez-Martínez et al. 2013, only considering NLAGN), but smaller than those obtained by Lemaux et al. (2010) from $[OII]$ and $H\alpha$ measurements in two clusters at a higher redshift, RXJ1821.6+6827 at $z \approx 0.82$ and Cl1604 at $z \approx 0.9$. These authors found that a fraction as large as $\sim 68\%$ of the objects can be classified as AGNs (Seyfert/LINER, using H97 boundaries), and that nearly half of the sample have $[OII]$ to $H\alpha$ equivalent width ratios higher than unity, the typical value observed for star-forming galaxies. The fraction of galaxies classified as AGN in their study was reduced to about 33% for blue galaxies. It is worth mentioning that the results from these authors are derived from a relatively small sample, 19 galaxies

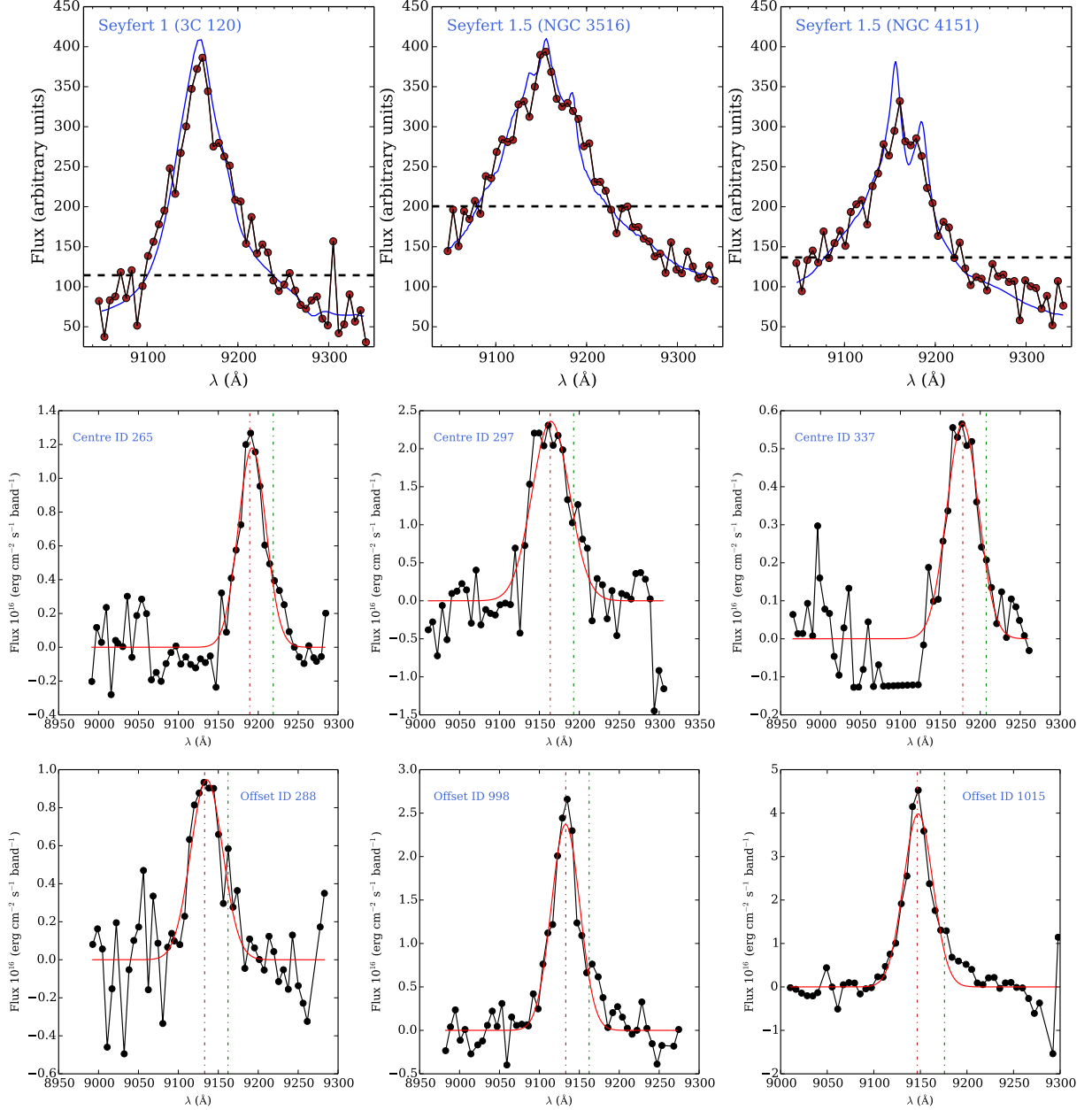


Fig. 10. In the top row, real spectra of local universe BLAGNs red-shifted to $z=0.395$ (blue solid line) and instances of the simulated pseudo-spectra (red dots and black continuum line) are shown. The dashed horizontal line marks the median value of the pseudo-spectra. See text for details. The middle and bottom rows show actual pseudo-spectra classified as BLAGN. The red and green vertical dash-dotted lines mark the positions of the H α and [N II] lines, respectively. The red solid line corresponds to the best fit to a Gaussian profile.

(out of a larger sample of 131 [O II] emitters) compared with ours (174 objects).

Furthermore, we have compared our result with the fraction of AGNs, computed with respect to the total number of cluster members brighter than a certain magnitude threshold, obtained by Martini et al. (2002) from a deep X-ray *Chandra* observation of the closer, massive cluster A2104 at $z=0.154$. They found 6 sources associated with red galaxies within the cluster whose X-ray properties are compatible with being AGN. Notably, only one of them shows optical features of an active nucleus. The authors conclude that at least $\geq 5\%$ of the cluster galaxies with $R < 20$ (the limiting magnitude of their counterparts) harbour an

AGN. In order to perform a rough comparison, we have determined the R-band magnitude distribution of our AGN sample using M05 broadband data. The limiting magnitude of the Martini et al. (2002) counterparts corresponds to $R = 22.3$ at the redshift of Cl0024. This value corresponds almost exactly with the peak of the R-band magnitude distribution of our AGNs. Within our sample, 45 AGNs have $R \leq 22.3$. We have determined the number of galaxies in the M05 catalogue with $R \leq 22.3$ in the redshift interval $0.35 < z < 0.45$ (both spectroscopic and photometric), within the same area of our AGN sample, obtaining 263 sources. Hence, a crude estimate of the fraction of AGNs within our sample would be $45/263 \approx 17\%$, i.e. more than three times

larger than the fractions obtained by means of X-ray estimates. However, once again it must be noticed that the X-ray sample is much smaller (and shallower) than ours, and hence the result should be considered with care. Actually our fraction of AGNs is similar to that obtained by Lemaux et al. (2010), 20% at $z \approx 0.9$. This suggests a lack of redshift evolution of the population of faint AGNs in the range $0.4 \lesssim z \lesssim 0.9$, or at least much milder than that predicted by Martini et al. (2009) for luminous AGNs, $f \sim (1+z)^{5.3}$.

The average of our AGN luminosity distribution (with no extinction correction) is $\log L(H\alpha) \approx 41.0$. At the bright end, we found one AGN with $\log L(H\alpha) \approx 41.7$, that corresponds to $\log L_X \sim 43$ using the $L(H\alpha)$ to L_X relation from Ho et al. (2001). This detection is compatible with the results from Martini et al. (2009) in the $0.3 < z < 0.6$ bin (four AGNs in ten clusters with $\log L_X \geq 43$).

We have cross-matched our ELG catalogue with a list of source detection positions from a *Chandra* ACIS-S observation of 40 ksec performed in FAINT mode, kindly provided to us by P. Tozzi. Five sources (out of 37) have been ascribed to the cluster after cross-matching the X-ray emitter list with the catalogue of spectroscopic redshifts from M05. From these, 3 sources have been detected as ELG in our survey and have been classified as pure AGN or composite according to the $[NII]/H\alpha$ ratio. The remaining 2 sources are detected in our deep TF images but their pseudo-spectra do not show emission line features at a significant level of detection.

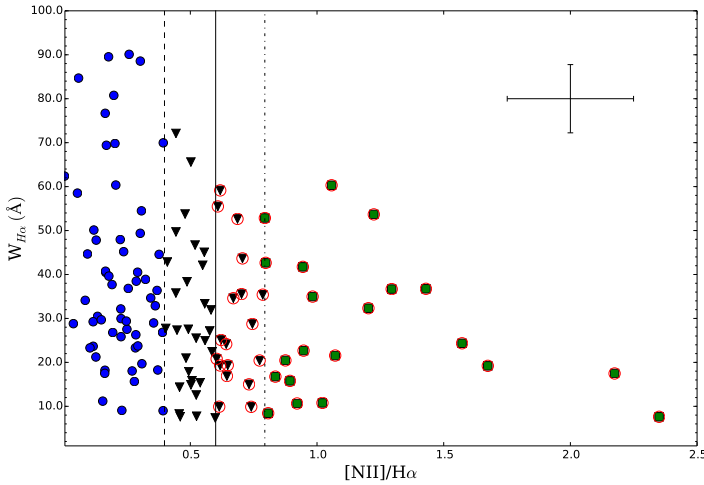


Fig. 11. EW α n2 diagram showing pure SF galaxies according to S06 criterion (blue dots), pure K01 AGN (green squares) and composite SF+AGN objects (black triangles). Classical AGNs as defined by H97 are denoted by open red circles. The dashed vertical line corresponds to S06 separation criterion, the solid one to the H97 boundary and finally the dashed-dotted line marks the K01 boundary. The error bars in the top right corner correspond to the median errors within our sample of ELG.

For the H97 SF galaxies, we have computed the star formation rate (SFR) using the standard assumption of 1 magnitude of extinction at the $H\alpha$ line (Kennicutt 1992, in a forthcoming paper a more realistic estimation will be done using the Balmer decrement computed with the $H\beta$ flux) and applying the standard luminosity-SFR conversion from Kennicutt (1998). The histogram of the SFR distribution is depicted in Fig. 5 (right

panel). The SFR peaks at $0.8 M_{\odot} \text{ yr}^{-1}$ with a median value of $1.4 M_{\odot} \text{ yr}^{-1}$.

The spatial distribution of AGN and SF galaxies in the radial velocity/projected cluster-centric distance space is depicted in Fig. 8. The very central region ($r \lesssim 250$ Kpc) is almost devoid of ELG, indicating an almost complete quenching of the star formation or AGN activity. AGNs are observed in both cluster components (A and B as defined in sect. 6), but are more abundant in the main structure. Beyond this point, the analysis of the distribution of galaxies relative to the cluster-centric distance has a limited validity, since on the one hand it does not account for the limited area coverage of our observations at large radii, and on the other it does not provide information of the importance of star formation or AGN activity relative to the density of galaxies in the surrounding environment. A thorough analysis of the dependency of the SFR and specific SFR with the local galaxy density (characterised by the Σ_5 parameter) will be presented in Pérez-Martínez et al. (in prep.).

Finally, we have plotted the colour-magnitude diagram (CMD) for the ELG sample, along with a control sample of cluster galaxies from M05. This control sample, comprising 792 galaxies, has been drawn from the main catalogue by choosing all the objects having valid BR photometry, within the same sky area as our sample and fulfilling $0.35 < z < 0.45$ (either spectroscopic or photometric). The K -correction has been applied to the M05 magnitudes by means of *kcorrect v4.2* (Blanton & Roweis 2007). The rest-frame $B - R$ vs. R CMD is depicted in Fig. 12. The bi-modality in the distribution of optical colours is clearly noticed, with a red sequence well developed. We have defined a boundary between the red sequence and the blue cloud as the intersection of the Gaussian functions resulting from the fit to each colour peak ($B - R = 1.39$). We have investigated the colour distributions of AGNs and SF galaxies (right panel in Fig. 12). The differences are not outstanding but noticeable. The Kolmogorov-Smirnov test rejects the null hypothesis that both samples are drawn from the same distribution with a p -value of 0.09. The colour distribution of SF galaxies reaches a clear maximum in the blue cloud, with a tail towards the red sequence region (either due to dust absorption or to the presence of old, red stellar populations), while the AGN colour distribution tends to peak at the boundary between the two regions, the so-called ‘green valley’, as expected for the population of galaxies hosting active nuclei (see for instance Pović et al. 2012, and references therein).

9. Cluster dynamics from emission line galaxies

As a final test of the reliability and usefulness of our data beyond the main drivers of the GLACE survey, we have applied the caustic technique (Diaferio & Geller 1997; Diaferio 1999) using the *CausticApp* code (Serra & Diaferio, in prep.) to explore the possibility of using ELG radial velocity data to trace the cluster mass. This method, unlike the traditional Jeans approach, does not rely on the assumption of dynamical equilibrium, and can be used to estimate the cluster mass even in non-equilibrium regions. Thus, in principle, it is well suited to be applied to ELGs, that are likely not in dynamical equilibrium.

To briefly summarise the physical idea behind the caustic technique, we will follow Serra et al. (2011): in hierarchical clustering models of structure formation, clusters form by the aggregation of smaller systems. This accretion does not take place purely radially, but particles within the falling clumps have velocities with a substantial non-radial component. The rms velocity $\langle v^2 \rangle$ is due to the gravitational potential of the cluster and the

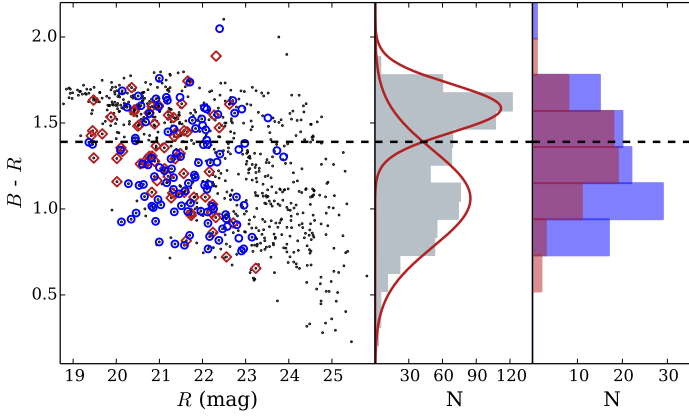


Fig. 12. *Left:* $B - R$ vs. R colour–magnitude diagram. The AGN are represented by red diamond symbols, while blue circles are SF galaxies. The black dots represent the cluster control sample from M05. The dashed line corresponds to the separation between the red sequence and blue cloud populations (see text). *Middle:* histogram of the control sample. The bi-modality of the distribution of optical colours is evident. The red curves are the best Gaussian fits to the distribution *Right:* colour histograms for AGNs (red) and SF (blue) galaxies. It is likely that both populations are drawn from different distributions.

groups where the galaxies reside, and to the tidal fields of the surrounding region.

In a redshift diagram (i.e. line-of-sight velocity v_{los} vs. projected distance to the center R_p), cluster galaxies populate a region with a characteristic trumpet shape with decreasing amplitude $\mathcal{A}(R_p)$ with increasing R_p . This amplitude is related to $\langle v^2 \rangle$. Diaferio & Geller (1997) identified this amplitude with the average component along the line of sight of the escape velocity at the three-dimensional radius $r = R_p$. The projection along the line of sight involves a function which depends on the anisotropy parameter $\beta(r) = 1 - (\langle v_\theta^2 \rangle + \langle v_\phi^2 \rangle) / 2\langle v_r^2 \rangle$. Here, $\langle v_\theta^2 \rangle$, $\langle v_\phi^2 \rangle$ and $\langle v_r^2 \rangle$ are the longitudinal, azimuthal and radial components of the velocity \mathbf{v} of a galaxy, respectively and the brackets represent the average over a local volume at a given position \mathbf{r} . Considering the cluster rotation negligible, $\langle v_\theta^2 \rangle = \langle v_\phi^2 \rangle = \langle v_{los}^2 \rangle$, where $\langle v_{los}^2 \rangle$ is the line-of-sight component of the velocity.

Following the results of Diaferio & Geller (1997), the square of the caustic amplitude $\mathcal{A}^2(r) = \langle v_{esc,los}^2 \rangle$ and relating the escape velocity to the cluster gravitational potential as $\langle v_{esc}^2 \rangle = -2\phi(r)$, it can be shown that

$$GM(< r) = \int_0^r \mathcal{A}^2(r) g(\beta) \mathcal{F}(r) dr \quad (13)$$

where $\mathcal{F}(r) = -2\pi G \rho(r) r^2 / \phi(r)$, with $\rho(r)$ the mass density profile and $g(\beta) = (3 - 2\beta(r)) / (1 - \beta(r))$. In order to solve Eq. 13, it is assumed that the product $\mathcal{F}_\beta(r) = \mathcal{F}(r) g(\beta)$ varies slowly with r , and hence it is possible to replace it by a constant parameter \mathcal{F}_β . It is easy to show that $\mathcal{F}(r)$ is a slowly varying function of r in hierarchical clustering scenarios. The assumption that $\mathcal{F}_\beta(r)$ is also a slow function of r , is somewhat stronger and is demonstrated in Serra et al. (2011).

Therefore, the mass profile could be estimated as:

$$GM(< r) = \mathcal{F}_\beta \int_0^r \mathcal{A}^2(r) dr. \quad (14)$$

The **CausticApp** is a graphical interface that allows an easy use of the caustic technique. The technique uses a binary tree according to a hierarchical method to arrange the galaxies in a catalogue according to their projected binding energy. By cutting the tree at the appropriate thresholds (details in Serra et al. 2011), it provides a set of candidate members, the cluster centre, velocity dispersion and size. With that information a redshift diagram is created and the caustics located. Finally, the caustic mass profile is estimated.

We have run the code with our complete data set of 174 ELGs, setting a conservative filling factor $\mathcal{F}_\beta = 0.5$. The center of the cluster computed by the code is $\alpha_{ELG} = 0^h 26^m 40.8^s$, $\delta_{ELG} = 17^\circ 9' 21.6''$ and the final members are 121. The redshift diagram with the location of the caustics and the cluster mass profile are depicted in the left and right panels of Fig. 13, respectively.

Fig. 13 also shows other two mass profiles estimated from ZwCl 0024.0+1652 data: a weak-lensing mass profile from Kneib et al. (2003) and another caustic mass profile, obtained with the larger galaxy catalog with 333 galaxies within the redshift range $z=[0.35, 0.45]$, used by Diaferio et al. (2005). For this analysis we kept the cluster center used in Diaferio et al. (2005): $\alpha_{D05} = 0^h 26^m 45.9^s$, $\delta_{D05} = 17^\circ 9' 41.1''$. The number of members identified in this case is 251. Despite the number difference, our sample is able to yield a very good estimate of the center. Indeed, the offset between $(\alpha_{ELG}, \delta_{ELG})$ and $(\alpha_{D05}, \delta_{D05})$ is negligible.

The agreement among all of the three mass profiles is remarkable at $r=[1, 2.3] \text{ Mpc } h^{-1}$. In the inner regions, the ELG-caustic mass profile is considerably lower than the other two, due to lack of galaxies in the very central regions of the cluster. In most clusters ELGs avoid the cluster center, which translates into a caustic amplitude that tends to underestimate the mass profile in the inner regions. As the mass profile is cumulative, this underestimate propagates into the final mass estimates. However, the cumulative caustic mass profile from ELGs in Fig 13 shows that the central mass does not contribute substantially to the total cluster mass at large radii. This suggests that in this cluster the velocity field is well sampled by the ELGs in the outskirts; consequently, the ELG-caustic mass profile is consistent with the estimates from previous studies.

With the caustic method, we derive $r_{200} = (1.21 \pm 0.1) \text{ Mpc } h^{-1}$ and $M_{200} = (4.1 \pm 0.2) \times 10^{14} \text{ M}_\odot h^{-1}$, where the uncertainties are due to the uncertainties in the mass profile. For comparison, Kneib et al. (2003), from weak-lensing analysis, derived $r_{200} = (1.19 \pm 0.9) \text{ Mpc } h^{-1}$ and $M_{200} = (3.97^{+0.8}_{-0.7}) \times 10^{14} \text{ M}_\odot h^{-1}$. Therefore, there is very good agreement between our results and those obtained by means of a radically different approach.

10. Summary and Conclusions

Aimed at exploring the technical feasibility of the GLACE project, we have carried out a TF survey of the intermediate redshift cluster ZwCl 0024.0+1652 (Cl0024 hereafter) at $z = 0.395$, targetting the H α /[N II] line complex. We have performed two pointings, covering approximately 2 virial radii and a velocity field of approximately $\pm 4000 \text{ km s}^{-1}$. Cl0024 is a very well studied cluster, and hence a good test bench to explore the capabilities, performance and limitations of the TF tomography method. In this paper we present the main technical aspects related to the creation of the catalogue of H α emitters, along with some simulations aimed at confirming the validity (and limitations) of our methods. We present a set of scientific results that can be used as

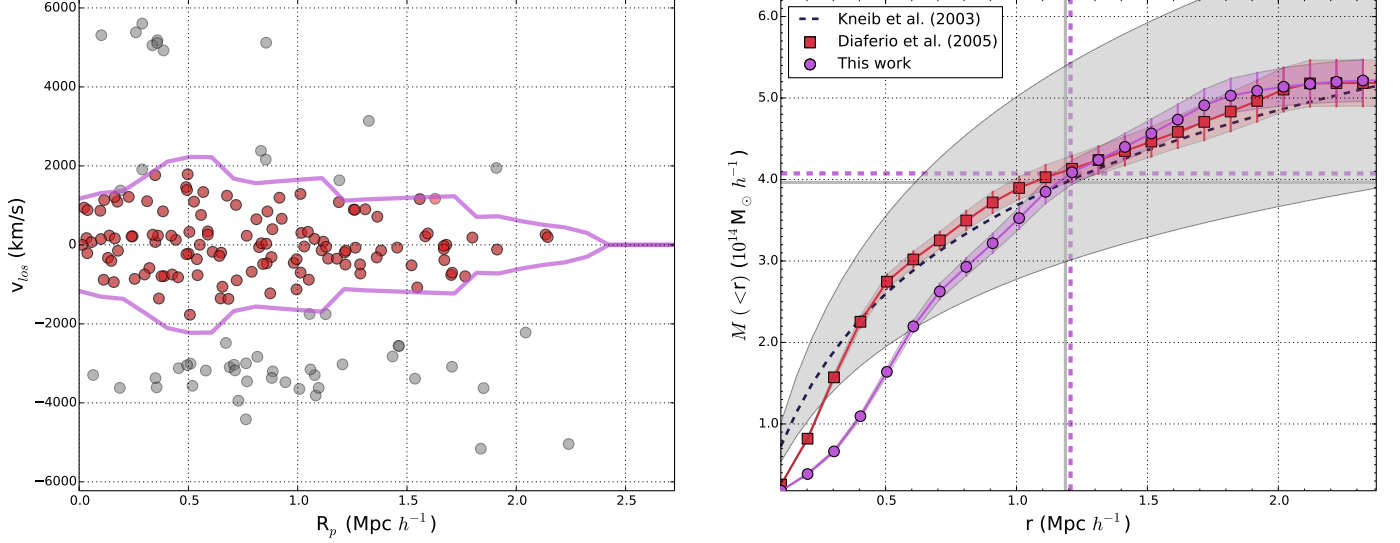


Fig. 13. *Left:* redshift diagram showing the selected cluster members (red dots, coincident with those in the main structure identified in sect. 6) and the caustics (purple solid lines). *Right:* caustic-ELG mass profile (purple circles) computed by integrating the squared caustic amplitude profile; NFW-best-fit mass profile to the weak-lensing mass from Kneib et al. (2003) (black dashed line); caustic analysis of the catalog from Diaferio et al. (2005) (red squares). The vertical and horizontal lines are M_{200} and r_{200} of the caustic-ELG (purple) and weak-lensing (grey) mass profiles.

a benchmark of the performance of our techniques upon comparison with previous works. These results include the spatial and redshift distribution of cluster galaxies, the $H\alpha$ luminosity function, the population of star-forming (SF) galaxies and AGNs and finally, an attempt to make estimations on the mass and velocity dispersion of the cluster based on our emission-line data. The main results are:

- A catalogue of 174 unique cluster emitters has been compiled. The completeness limit of our $H\alpha$ line sample is $f_{H\alpha} \sim 0.9 \times 10^{-16} \text{ erg s}^{-1} \text{ cm}^{-2}$, a flux consistent or below the GLACE requirement.
- We have compared our redshift estimates for our galaxies, as given by the $H\alpha$ line position in the pseudo-spectra, with spectroscopic redshifts from Moran et al. (2005). There is an excellent agreement: the redshift error defined as $|z_{TF} - z_{spec}|/(1 + z_{spec})$ is on average 0.002 (median value 0.0005) with a maximum value of 0.02. Hence, we can consider the TF-derived redshifts as of spectroscopic quality.
- The redshift distribution of the cluster galaxies allows us to identify two interacting structures already identified in spectroscopic surveys (Czoske et al. 2002). Moreover, we suggest the existence of a third interacting group (previously not identified as such, but as part of the surrounding field galaxy population), although the clustering of the sources can be due to an instrumental effect (uneven spatial coverage at the shortest and longest wavelengths).
- The $H\alpha$ luminosity function is well aligned with previous estimates from Kodama et al. (2004) up to the completeness limit of the sample, $\log L(H\alpha + [N II]) \text{ (erg s}^{-1}) \approx 41$.
- Broad-line AGNs (BLAGN) can be separated from narrow-line ones (NLAGN) or SF galaxies. In order to select candidates to BLAGN we have performed simple Gaussian fits to the pseudo-spectra, arriving to a final list of 25 robust candidates, i.e. 14% of the sample of ELGs. Furthermore, our observing technique allowed us to deblend the $H\alpha$ and

$[N II]$ lines. In fact, in an outstanding fraction of the objects, both lines appear clearly separated even in a visual inspection of the pseudo-spectra. We have used this deblending capability to discriminate the population of NLAGNs from the SF galaxies. The fraction of NLAGNs depends on the criterion used. If a ‘classical’ separation criterion is applied (Ho et al. 1997, H97), the fraction of NLAGNs is $\sim 22\%$. The total fraction of AGN (BLAGN+NLAGN) is $\sim 37\%$ or around 17% of the cluster population brighter than $R = 22.3$, similar to estimates derived $[O II]$ observations $z \approx 0.9$. This suggests a lack of redshift evolution of the population of faint AGNs in the range $0.4 \lesssim z \lesssim 0.9$, or at least much milder than previous predictions.

- The star formation rate (SFR), computed using the standard assumption of 1 magnitude of extinction at the $H\alpha$ line and the standard luminosity-SFR conversion from Kennicutt (1998), peaks at $0.8 M_{\odot} \text{ yr}^{-1}$ with a median value of $1.4 M_{\odot} \text{ yr}^{-1}$.
- We have found that the innermost region of the cluster ($r \lesssim 250 \text{ Kpc}$) is virtually devoid of ELGs, indicating an almost complete quenching of the star formation and AGN activity, as expected for a cluster at this redshift.
- We have used the dynamical information (radial velocities) provided by our ELGs to estimate the mass, radius and velocity dispersion of C10024 using the technique of caustics in the redshift space Diaferio & Geller (1997); Diaferio (1999) as implemented in the CausticApp application from Serra et al. (2011). With the caustic method, we derive $r_{200} = (1.21 \pm 0.1) \text{ Mpc } h^{-1}$ and $M_{200} = (4.1 \pm 0.2) \times 10^{14} M_{\odot} h^{-1}$, in very good agreement with the weak-lensing estimate from Kneib et al. (2003).

The results outlined above indicate that the TF tomography technique is a powerful tool for the proposed research and that the devised observing methods and reduction and analysis procedures yield results that meet or exceed the GLACE requirements.

The tunable filters of the OSIRIS instrument at the 10.4m GTC telescope constitute a powerful tool to explore galaxy cluster, allowing to derive important properties of the members, and even to investigate the cluster dynamics.

References

- Alloin, D., Collin-Souffrin, S., Joly, M., & Vigroux, L. 1979, *A&A*, 78, 200
- Altieri, B., Berta, S., Lutz, D., et al. 2010, *A&A*, 518, L17
- Arribas, S., Mediavilla, E., García-Lorenzo, B., & del Burgo, C. 1997, *ApJ*, 490, 227
- Baldwin, J. A., Phillips, M. M., & Terlevich, R. 1981, *PASP*, 93, 5
- Balogh, M. L., Morris, S. L., Yee, H. K. C., Carlberg, R. G., & Ellingson, E. 1999, *ApJ*, 527, 54
- Balogh, M. L., Navarro, J. F., & Morris, S. L. 2000, *ApJ*, 540, 113
- Bertin, E. & Arnouts, S. 1996, *A&AS*, 117, 393
- Blanton, M. R. & Roweis, S. 2007, *AJ*, 133, 734
- Bruzual, G. & Charlot, S. 2003, *MNRAS*, 344, 1000
- Butcher, H. & Oemler, Jr., A. 1984, *ApJ*, 285, 426
- Calzetti, D., Armus, L., Bohlin, R. C., et al. 2000, *ApJ*, 533, 682
- Cepa, J., Aguiar, M., Castañeda, H. O., et al. 2003, in *Revista Mexicana de Astronomía y Astrofísica Conference Series*, Vol. 16, *Revista Mexicana de Astronomía y Astrofísica Conference Series*, ed. J. M. Rodríguez Espinoza, F. Garzon Lopez, & V. Melo Martin, 13–18
- Cepa, J., Aguiar, M., Castañeda, H. O., et al. 2005, in *Revista Mexicana de Astronomía y Astrofísica Conference Series*, Vol. 24, *Revista Mexicana de Astronomía y Astrofísica Conference Series*, ed. A. M. Hidalgo-Gómez, J. J. González, J. M. Rodríguez Espinoza, & S. Torres-Peimbert, 1–6
- Cepa, J., Bongiovanni, A., Pérez García, A. M., et al. 2013, in *Revista Mexicana de Astronomía y Astrofísica Conference Series*, Vol. 42, *Revista Mexicana de Astronomía y Astrofísica Conference Series*, 70–72
- Chabrier, G. 2003, *PASP*, 115, 763
- Cid Fernandes, R., Stasińska, G., Schlickmann, M. S., et al. 2010, *MNRAS*, 403, 1036
- Coia, D., Metcalfe, L., McBreen, B., et al. 2005, *A&A*, 430, 59
- Czoske, O., Moore, B., Kneib, J., & Soucaill, G. 2002, *A&A*, 386, 31
- Denicoló, G., Terlevich, R., & Terlevich, E. 2002, *MNRAS*, 330, 69
- Diaferio, A. 1999, *MNRAS*, 309, 610
- Diaferio, A. & Geller, M. J. 1997, *ApJ*, 481, 633
- Diaferio, A., Geller, M. J., & Rines, K. J. 2005, *ApJ*, 628, L97
- Dressler, A. 1980, *ApJ*, 236, 351
- Dressler, A., Oemler, Jr., A., Couch, W. J., et al. 1997, *ApJ*, 490, 577
- Fernández Lorenzo, M., Cepa, J., Bongiovanni, A., et al. 2009, *A&A*, 496, 389
- Filippenko, A. & Greenstein, J. L. 1984, *PASP*, 96, 530
- García-Lorenzo, B., Sánchez, S. F., Mediavilla, E., González-Serrano, J. I., & Christensen, L. 2005, *ApJ*, 621, 146
- Geach, J. E., Smail, I., Ellis, R. S., et al. 2006, *ApJ*, 649, 661
- González, J. J., Cepa, J., González-Serrano, J. I., & Sánchez-Portal, M. 2014, *MNRAS*, 443, 3289
- Haines, C. P., Pereira, M. J., Smith, G. P., et al. 2013, *ApJ*, 775, 126
- Haines, C. P., Smith, G. P., Egami, E., et al. 2009, *ApJ*, 704, 126
- Ho, L. C., Feigelson, E. D., Townsley, L. K., et al. 2001, *ApJ*, 549, L51
- Ho, L. C., Filippenko, A. V., & Sargent, W. L. W. 1997, *ApJS*, 112, 315
- Ilbert, O., Arnouts, S., McCracken, H. J., et al. 2006, *A&A*, 457, 841
- Ilbert, O., Capak, P., Salvato, M., et al. 2009, *ApJ*, 690, 1236
- Jones, D. H. & Bland-Hawthorn, J. 2001, *ApJ*, 550, 593
- Jones, D. H., Shopbell, P. L., & Bland-Hawthorn, J. 2002, *MNRAS*, 329, 759
- Kaspi, S., Maoz, D., Netzer, H., et al. 1996, *ApJ*, 470, 336
- Kauffmann, G., Heckman, T. M., Tremonti, C., et al. 2003, *MNRAS*, 346, 1055
- Kauffmann, G., White, S. D. M., Heckman, T. M., et al. 2004, *MNRAS*, 353, 713
- Kennicutt, Jr., R. C. 1992, *ApJ*, 388, 310
- Kennicutt, Jr., R. C. 1998, *ARA&A*, 36, 189
- Kewley, L. J., Dopita, M. A., Sutherland, R. S., Heisler, C. A., & Trevena, J. 2001, *ApJ*, 556, 121
- Kneib, J., Hudelot, P., Ellis, R. S., et al. 2003, *ApJ*, 598, 804
- Kodama, T., Balogh, M. L., Smail, I., Bower, R. G., & Nakata, F. 2004, *MNRAS*, 354, 1103
- Kodama, T., Bell, E. F., & Bower, R. G. 1999, *MNRAS*, 302, 152
- Kodama, T. & Bower, R. G. 2001, *MNRAS*, 321, 18
- Koyama, Y., Kodama, T., Nakata, F., Shimasaku, K., & Okamura, S. 2011, *ApJ*, 734, 66
- Koyama, Y., Kodama, T., Shimasaku, K., et al. 2010, *MNRAS*, 403, 1611
- Lara-López, M. A., Cepa, J., Castañeda, H., et al. 2010, *PASP*, 122, 1495
- Lemaux, B. C., Lubin, L. M., Shapley, A., et al. 2010, *ApJ*, 716, 970
- Madau, P., Pozzetti, L., & Dickinson, M. 1998, *ApJ*, 498, 106
- Martini, P., Kelson, D. D., Mulchaey, J. S., & Trager, S. C. 2002, *ApJ*, 576, L109
- Martini, P., Miller, E. D., Brodwin, M., et al. 2013, *ApJ*, 768, 1
- Martini, P., Sivakoff, G. R., & Mulchaey, J. S. 2009, *ApJ*, 701, 66
- Miller, C. J., Nichol, R. C., Gómez, P. L., Hopkins, A. M., & Bernardi, M. 2003, *ApJ*, 597, 142
- Monet, D. G., Levine, S. E., Canzian, B., et al. 2003, *AJ*, 125, 984
- Moran, S. M., Ellis, R. S., Treu, T., et al. 2005, *ApJ*, 634, 977
- Moran, S. M., Ellis, R. S., Treu, T., et al. 2007, *ApJ*, 671, 1503
- Oke, J. B. 1974, *ApJS*, 27, 21
- Oke, J. B. 1990, *AJ*, 99, 1621
- Pagel, B. E. J., Edmunds, M. G., Blackwell, D. E., Chun, M. S., & Smith, G. 1979, *MNRAS*, 189, 95
- Pascual, S., Gallego, J., & Zamorano, J. 2007, *PASP*, 119, 30
- Pérez-Martínez, R., Sánchez-Portal, M., Pintos-Castro, I., et al. 2013, *Astronomische Nachrichten*, 334, 458
- Pimbblet, K. A., Smail, I., Edge, A. C., et al. 2001, *MNRAS*, 327, 588
- Pintos-Castro, I., Sánchez-Portal, M., Cepa, J., et al. 2013, *A&A*, 558, A100
- Poggianti, B. M., Smail, I., Dressler, A., et al. 1999, *ApJ*, 518, 576
- Popesso, P. & Biviano, A. 2006, *A&A*, 460, L23
- Popesso, P., Biviano, A., Romaniello, M., & Böhringer, H. 2007, *A&A*, 461, 411
- Pović, M., Sánchez-Portal, M., Pérez García, A. M., et al. 2012, *A&A*, 541, A118
- Rousselot, P., Lidman, C., Cuby, J.-G., Moreels, G., & Monnet, G. 2000, *A&A*, 354, 1134
- Roy, J.-R., Arsenault, R., & Joncas, G. 1986, *ApJ*, 300, 624
- Serra, A. L., Diaferio, A., Murante, G., & Borgani, S. 2011, *MNRAS*, 412, 800
- Skrutskie, M. F., Cutri, R. M., Stiening, R., et al. 2006, *AJ*, 131, 1163
- Sorrentino, G., Radovich, M., & Rifatto, A. 2006, *A&A*, 451, 809
- Stasińska, G., Cid Fernandes, R., Mateus, A., Sodré, L., & Asari, N. V. 2006, *MNRAS*, 371, 972
- Taylor, M. B. 2005, in *Astronomical Society of the Pacific Conference Series*, Vol. 347, *Astronomical Data Analysis Software and Systems XIV*, ed. P. Shopbell, M. Britton, & R. Ebert, 29
- Treu, T., Ellis, R. S., Kneib, J., et al. 2003, *ApJ*, 591, 53
- Veilleux, S. & Osterbrock, D. E. 1987, *ApJS*, 63, 295
- Webb, T. M. A., O'Donnell, D., Yee, H. K. C., et al. 2013, *AJ*, 146, 84
- Zhang, Y.-Y., Böhringer, H., Mellier, Y., Soucaill, G., & Forman, W. 2005, *A&A*, 429, 85

Table 5. Catalogue of unique ELGs of Cl0024. The identifiers with 'C' correspond to sources gathered from the central pointing, while those with 'O' correspond to sources gathered from the offset one.

ID	RA J2000 (00:26:ss.ss)	Dec J2000 (+17:mm:ss.s)	z	$f_{H\alpha} 10^{-17}$ (erg cm $^{-2}$ s $^{-1}$)	$f_{[NII]} 10^{-17}$ (erg cm $^{-2}$ s $^{-1}$)	EW $_{H\alpha}$ (Å)	EW $_{H\alpha+[NII]}$ (Å)	Type
4_C	34.27	06:04.5	0.3820	33±6	2±2	84.7	88.9	SF
12_C	42.98	06:12.2	0.3999	18±6	-	38.9	-	BLAGN
24_C	28.93	06:20.8	0.3982	7±3	5±3	9.9	15.6	NLAGN
35_C	23.84	06:26.9	0.3955	10±6	4±4	9.0	12.3	SF
60_C	38.72	06:46.9	0.3967	12±3	-	42.3	-	SF
70_C	29.05	06:59.1	0.3785	10±4	5±7	17.9	26.4	SF
72_C	19.39	07:03.0	0.3993	35±11	18±10	17.4	26.6	BLAGN
73_C	42.31	07:04.7	0.3949	7±2	8±2	36.7	87.2	NLAGN
87_C	14.95	07:14.5	0.3803	13±5	14±8	21.6	43.6	NLAGN
96_C	34.49	07:15.4	0.3832	37±11	-	35.5	-	SF
97_C	34.88	07:15.4	0.4014	10±3	5±3	14.9	22.3	SF
105_C	14.79	07:19.8	0.3832	60±14	-	62.4	-	SF
106_C	30.99	07:22.0	0.3807	25±7	6±4	30.0	36.5	SF
138_C	34.22	07:42.8	0.3812	33±8	12±6	36.4	49.3	SF
143_C	39.26	07:46.5	0.3784	14±4	1±3	34.1	36.9	SF
147_C	41.17	07:47.0	0.3888	13±3	2±2	40.5	46.5	SF
153_C	21.48	07:55.0	0.3774	16±5	11±5	43.7	75.2	NLAGN
163_C	44.93	08:10.1	0.3955	25±18	22±19	6.7	12.7	BLAGN
193_C	40.10	08:21.8	0.4008	6±2	4±5	15.0	26.0	NLAGN
196_C	27.09	08:23.8	0.3812	15±6	13±9	15.8	30.0	NLAGN
200_C	42.90	08:23.8	0.3962	11±3	8±5	35.6	58.8	NLAGN
219_C	29.81	08:36.4	0.3993	59±15	21±10	62.1	81.3	BLAGN
224_C	16.48	08:40.3	0.3943	7±1	2±2	44.6	59.5	SF
227_C	35.73	08:40.6	0.4003	13±3	16±7	32.3	70.4	NLAGN
246_C	23.79	08:49.9	0.4002	17±6	5±9	15.7	20.0	SF
253_C	23.79	08:50.2	0.3810	19±4	6±3	54.5	69.7	SF
255_C	38.29	08:51.4	0.4007	7±2	3±1	49.7	70.0	SF
263_C	27.70	08:51.5	0.3991	48±9	30±11	59.1	90.7	NLAGN
265_C	33.82	08:56.0	0.4002	16±3	8±3	47.7	67.8	BLAGN
280_C	33.83	08:56.6	0.3910	11±3	11±6	22.7	44.0	NLAGN
285_C	18.64	08:57.1	0.3935	101±14	5±3	425.6	437.2	SF
287_C	18.63	08:57.1	0.3942	42±15	12±8	23.3	29.9	SF
290_C	42.37	09:02.2	0.3798	6±3	4±2	16.9	28.0	SF
293_C	30.79	09:02.5	0.4008	4±1	7±3	24.3	62.9	NLAGN
297_C	11.22	09:02.7	0.3962	31±12	32±21	12.1	24.5	NLAGN
303_C	30.80	09:02.9	0.3870	5±2	-	28.3	-	BLAGN
308_C	37.99	09:04.4	0.3995	40±7	8±4	69.8	82.3	SF
314_C	41.09	09:05.3	0.3959	6±2	1±2	30.5	34.5	SF
317_C	19.72	09:10.2	0.4009	10±3	6±2	22.4	35.6	SF
320_C	40.69	09:11.9	0.4002	14±3	-	89.2	-	SF
322_C	43.27	09:12.6	0.4034	9±3	-	35.5	-	SF
323_C	43.79	09:14.3	0.3959	8±2	-	64.4	-	SF
332_C	34.29	09:14.5	0.3811	23±5	9±5	70.0	92.1	SF
337_C	30.97	09:14.7	0.3985	7±2	5±2	81.3	128.9	BLAGN
338_C	40.31	09:15.7	0.3915	28±9	14±10	15.8	23.9	SF
339_C	31.64	09:16.0	0.3902	13±4	4±2	38.5	48.8	SF
341_C	28.14	09:16.1	0.3937	27±8	21±16	20.4	36.7	NLAGN
343_C	15.28	09:17.8	0.3992	30±6	18±5	55.5	90.5	NLAGN
345_C	18.26	09:17.9	0.3955	18±5	10±4	25.5	38.4	SF
353_C	18.25	09:17.9	0.3951	10±2	5±2	38.4	55.6	SF
358_C	15.25	09:18.2	0.4193	8±3	-	26.5	-	SF
359_C	41.15	09:18.6	0.4202	16±5	-	48.9	-	SF
364_C	28.52	09:20.5	0.4212	7±3	-	35.7	-	SF
366_C	28.52	09:20.9	0.3992	67±12	17±8	90.1	109.3	SF
374_C	31.31	09:22.4	0.4187	6±3	-	12.8	-	SF
382_C	33.50	09:23.7	0.4040	8±2	4±3	25.0	38.3	SF
388_C	40.08	09:24.1	0.3783	11±3	1±2	58.5	61.5	SF
405_C	32.32	09:24.2	0.3936	114±30	66±24	27.1	42.1	SF
408_C	33.51	09:24.3	0.3943	70±25	34±14	21.0	31.2	NLAGN
409_C	35.93	09:24.5	0.3958	26±16	21±12	8.4	15.2	SF
410_C	40.99	09:24.6	0.3930	11±4	2±5	18.2	21.0	SF
422_C	34.09	09:26.0	0.3933	67±14	37±12	45.1	68.1	SF
423_C	35.39	09:26.3	0.4199	14±5	-	38.3	-	SF
424_C	24.34	09:26.6	0.3908	51±10	21±9	42.8	59.1	SF
433_C	24.34	09:26.9	0.4004	13±3	2±2	47.8	53.2	SF

Table 5. continued.

ID	RA J2000 (00:26:ss.ss)	Dec J2000 (+17:mm:ss.s)	z	$f_{H\alpha}$ 10^{-17} (erg cm $^{-2}$ s $^{-1}$)	$f_{[NII]}$ 10^{-17} (erg cm $^{-2}$ s $^{-1}$)	EW $_{H\alpha}$ (Å)	EW $_{H\alpha+[NII]}$ (Å)	Type
437_C	39.84	09:28.7	0.4189	23 \pm 10	-	44.6	-	SF
443_C	42.44	09:32.2	0.3961	12 \pm 3	4 \pm 5	29.0	39.7	SF
450_C	34.55	09:32.8	0.3942	12 \pm 3	3 \pm 2	45.2	55.0	SF
451_C	35.48	09:36.0	0.3911	25 \pm 7	5 \pm 4	26.8	31.8	SF
452_C	44.08	09:37.9	0.3945	21 \pm 8	8 \pm 10	18.3	24.8	SF
453_C	39.85	09:45.5	0.4016	6 \pm 3	3 \pm 3	7.7	11.2	SF
456_C	24.84	09:47.2	0.3966	52 \pm 13	48 \pm 20	31.9	58.5	BLAGN
559_C	40.91	09:48.5	0.3870	7 \pm 3	9 \pm 6	10.1	23.0	BLAGN
560_C	18.15	09:48.7	0.3945	29 \pm 6	13 \pm 5	72.1	99.9	SF
571_C	18.15	09:48.7	0.3783	10 \pm 2	3 \pm 2	36.8	46.0	SF
574_C	38.61	09:50.9	0.3928	10 \pm 2	2 \pm 1	76.7	87.9	SF
575_C	42.63	09:51.2	0.3953	11 \pm 2	2 \pm 1	80.8	94.5	SF
582_C	41.37	09:51.4	0.3957	15 \pm 4	3 \pm 2	37.7	44.6	SF
612_C	34.45	09:52.2	0.3945	25 \pm 6	12 \pm 6	53.1	75.4	BLAGN
620_C	44.70	09:52.9	0.4062	9 \pm 5	2 \pm 4	9.1	11.1	SF
625_C	41.90	09:53.3	0.3964	5 \pm 2	1 \pm 1	29.3	32.6	SF
640_C	28.87	09:56.8	0.3930	11 \pm 3	3 \pm 5	27.5	34.4	SF
645_C	28.88	09:57.3	0.3794	20 \pm 5	3 \pm 2	89.5	103.2	SF
658_C	38.39	09:59.1	0.3950	7 \pm 2	6 \pm 3	35.4	64.9	NLAGN
659_C	36.85	10:00.2	0.3962	13 \pm 3	14 \pm 4	60.3	118.0	NLAGN
662_C	39.02	10:02.3	0.4181	9 \pm 3	-	30.9	-	SF
675_C	32.00	10:02.6	0.3941	72 \pm 15	22 \pm 8	49.4	63.3	SF
677_C	16.92	10:02.8	0.3914	51 \pm 19	41 \pm 38	13.3	24.0	BLAGN
687_C	22.02	10:05.6	0.3917	13 \pm 4	21 \pm 9	19.2	51.6	NLAGN
714_C	24.51	10:06.4	0.3962	27 \pm 6	14 \pm 4	46.7	69.9	SF
728_C	31.25	10:11.2	0.3935	15 \pm 4	14 \pm 5	46.1	84.5	BLAGN
730_C	28.51	10:12.5	0.3993	7 \pm 3	3 \pm 3	26.8	36.4	SF
748_C	31.07	10:16.4	0.3798	24 \pm 5	12 \pm 7	65.6	91.9	SF
758_C	24.84	10:21.9	0.3959	22 \pm 6	21 \pm 8	35.0	67.7	NLAGN
762_C	32.72	10:24.9	0.3945	10 \pm 3	4 \pm 2	27.7	38.7	SF
763_C	25.86	10:26.8	0.3746	15 \pm 8	36 \pm 21	7.6	26.5	NLAGN
772_C	25.87	10:27.1	0.3982	16 \pm 5	2 \pm 2	50.1	55.6	SF
773_C	33.90	10:27.2	0.3949	30 \pm 7	3 \pm 6	104.5	114.0	SF
775_C	33.91	10:27.7	0.3918	8 \pm 2	1 \pm 1	40.7	46.9	SF
777_C	30.83	10:29.1	0.3805	46 \pm 8	14 \pm 4	88.6	111.1	SF
783_C	30.84	10:29.6	0.4011	6 \pm 3	4 \pm 4	7.4	11.8	SF
794_C	25.97	10:30.1	0.3768	16 \pm 5	-	55.9	-	SF
811_C	37.98	10:31.3	0.4028	4 \pm 1	6 \pm 2	36.7	89.2	NLAGN
814_C	28.49	10:36.0	0.3782	7 \pm 3	-	28.8	-	SF
826_C	37.30	10:37.0	0.3962	33 \pm 7	26 \pm 9	52.9	91.5	NLAGN
850_C	12.84	10:37.1	0.3919	64 \pm 13	60 \pm 18	41.7	83.2	NLAGN
869_C	42.74	10:43.3	0.3948	11 \pm 3	6 \pm 3	30.5	48.3	BLAGN
872_C	33.63	10:45.7	0.3935	7 \pm 3	3 \pm 2	12.6	19.0	SF
875_C	43.49	10:47.0	0.3899	31 \pm 6	6 \pm 4	60.4	71.1	SF
882_C	22.10	10:49.1	0.4052	7 \pm 4	3 \pm 4	8.3	12.0	SF
884_C	28.79	10:49.9	0.3967	14 \pm 3	3 \pm 4	48.0	57.0	SF
886_C	28.80	10:50.2	0.3938	7 \pm 2	9 \pm 2	53.7	117.4	NLAGN
888_C	43.31	10:51.5	0.3888	17 \pm 3	11 \pm 5	52.6	90.6	NLAGN
889_C	41.50	11:02.3	0.3952	9 \pm 3	6 \pm 3	24.2	40.3	NLAGN
907_C	39.14	11:02.6	0.4190	15 \pm 5	-	55.5	-	SF
916_C	26.71	11:02.6	0.3836	4 \pm 1	1 \pm 1	26.3	33.2	SF
923_C	26.71	11:02.9	0.4035	4 \pm 2	2 \pm 3	7.7	11.8	SF
927_C	37.32	11:03.3	0.3967	34 \pm 7	27 \pm 8	42.7	78.8	NLAGN
929_C	26.38	11:04.7	0.3806	32 \pm 11	15 \pm 9	14.4	20.9	SF
935_C	26.37	11:05.1	0.3929	9 \pm 3	3 \pm 3	23.7	30.1	SF
938_C	36.58	11:08.1	0.3991	4 \pm 1	2 \pm 1	27.5	40.9	SF
948_C	35.16	11:08.4	0.3910	14 \pm 3	1 \pm 2	44.7	48.5	SF
953_C	35.16	11:09.0	0.3924	5 \pm 2	10 \pm 3	17.5	56.2	NLAGN
955_C	43.18	11:10.6	0.3910	9 \pm 3	5 \pm 4	19.3	32.0	NLAGN
966_C	22.81	11:13.1	0.3963	43 \pm 9	24 \pm 7	42.1	64.5	SF
977_C	30.98	11:14.2	0.3917	8 \pm 2	7 \pm 3	20.5	38.2	NLAGN
72_O	25.46	11:27.2	0.3962	27 \pm 4	6 \pm 3	33.0	39.7	BLAGN
102_O	24.51	11:30.1	0.4020	28 \pm 3	27 \pm 6	17.1	32.9	BLAGN
139_O	27.95	11:38.0	0.3869	14 \pm 2	3 \pm 2	25.9	31.5	SF
146_O	33.89	11:42.4	0.3913	20 \pm 2	12 \pm 3	51.9	80.1	BLAGN
247_O	25.21	11:47.6	0.4016	24 \pm 11	25 \pm 8	137.1	147.1	SF

Table 5. continued.

ID	RA J2000 (00:26:ss.ss)	Dec J2000 (+17:mm:ss.s)	z	$f_{H\alpha} 10^{-17}$ (erg cm $^{-2}$ s $^{-1}$)	$f_{[NII]} 10^{-17}$ (erg cm $^{-2}$ s $^{-1}$)	EW $_{H\alpha}$ (Å)	EW $_{H\alpha+[NII]}$ (Å)	Type
277_O	19.69	11:54.1	0.3928	9 \pm 2	6 \pm 3	34.6	57.0	NLAGN
278_O	19.68	11:54.4	0.3987	95 \pm 7	113 \pm 8	27.6	61.1	BLAGN
282_O	28.20	11:55.5	0.3802	9 \pm 1	1 \pm 1	23.7	26.4	SF
288_O	31.32	11:56.7	0.3916	9 \pm 1	6 \pm 1	16.8	27.2	BLAGN
291_O	25.68	12:05.4	0.3888	9 \pm 2	6 \pm 3	19.3	32.4	NLAGN
335_O	25.68	12:05.7	0.3941	9 \pm 1	8 \pm 3	10.6	19.9	NLAGN
336_O	33.64	12:19.7	0.3795	9 \pm 2	2 \pm 2	18.0	22.8	SF
381_O	07.54	12:29.9	0.3804	9 \pm 2	1 \pm 2	21.2	23.9	SF
384_O	31.25	12:32.1	0.3927	12 \pm 2	2 \pm 1	45.5	52.7	BLAGN
410_O	39.92	12:36.7	0.3810	7 \pm 2	6 \pm 3	16.8	30.9	NLAGN
457_O	20.48	12:45.4	0.3920	11 \pm 2	8 \pm 2	9.9	17.2	NLAGN
485_O	41.88	12:45.6	0.3935	10 \pm 1	6 \pm 1	31.9	50.7	SF
501_O	28.37	12:46.8	0.3790	7 \pm 1	1 \pm 1	11.2	12.9	SF
567_O	12.54	12:54.0	0.3970	10 \pm 2	6 \pm 2	25.1	39.8	NLAGN
568_O	37.59	12:54.3	0.3791	12 \pm 2	-	28.9	-	SF
647_O	18.28	13:01.0	0.3794	9 \pm 2	1 \pm 2	17.5	20.6	SF
651_O	26.98	13:03.7	0.3946	15 \pm 2	9 \pm 3	19.2	31.7	BLAGN
657_O	28.23	13:07.8	0.3894	16 \pm 2	7 \pm 3	27.3	39.5	SF
664_O	28.24	13:07.9	0.3953	15 \pm 2	9 \pm 2	20.8	33.7	NLAGN
689_O	09.06	13:16.1	0.4098	8 \pm 1	1 \pm 2	39.6	46.3	SF
700_O	14.38	13:19.9	0.3808	10 \pm 1	10 \pm 3	10.8	21.6	NLAGN
708_O	36.16	13:36.4	0.3965	7 \pm 1	2 \pm 2	19.7	25.5	SF
847_O	15.40	13:41.7	0.3964	38 \pm 7	-	51.9	-	SF
919_O	27.70	13:49.8	0.3952	14 \pm 2	3 \pm 2	29.4	36.5	SF
967_O	23.58	13:58.0	0.3783	8 \pm 1	-	27.8	-	SF
998_O	23.62	13:58.5	0.3916	28 \pm 2	26 \pm 5	38.5	71.1	BLAGN
1015_O	29.19	14:02.9	0.3937	47 \pm 3	14 \pm 4	40.5	51.5	SF
1039_O	29.14	14:03.0	0.3961	28 \pm 3	22 \pm 5	23.2	41.1	BLAGN
1057_O	41.25	14:04.2	0.3934	13 \pm 1	5 \pm 1	32.9	44.7	SF
1074_O	37.75	14:12.2	0.3711	21 \pm 2	12 \pm 5	33.4	51.1	SF
1097_O	08.54	14:58.7	0.3947	9 \pm 1	4 \pm 2	53.8	76.4	SF
1103_O	20.14	15:10.5	0.3960	9 \pm 2	1 \pm 2	29.7	34.0	SF
1125_O	08.95	15:10.7	0.3914	8 \pm 1	6 \pm 3	28.7	48.9	NLAGN
1130_O	24.16	15:27.5	0.3919	8 \pm 1	3 \pm 1	34.7	46.5	SF
1133_O	32.95	15:29.3	0.3717	15 \pm 3	2 \pm 4	23.3	25.7	SF
1157_O	20.26	15:32.5	0.4042	54 \pm 4	9 \pm 3	69.4	80.1	SF
1162_O	28.36	15:36.1	0.3848	78 \pm 8	34 \pm 9	29.4	41.4	BLAGN
1165_O	18.65	15:42.7	0.3950	17 \pm 2	9 \pm 2	15.4	23.8	SF
1168_O	24.75	15:48.8	0.4005	13 \pm 3	2 \pm 2	19.8	22.4	BLAGN
1173_O	30.79	15:53.9	0.3901	18 \pm 2	6 \pm 4	38.9	50.6	SF
1204_O	26.10	16:47.0	0.3948	9 \pm 2	2 \pm 2	32.2	38.8	SF
1219_O	13.33	16:54.8	0.3820	17 \pm 2	9 \pm 2	22.3	33.7	BLAGN
1220_O	20.28	17:03.5	0.4006	14 \pm 1	6 \pm 1	35.8	50.6	SF

Acknowledgements. We acknowledge the support provided by M. Balogh during the preparation of the GLACE proposal to ESO, as well as his useful suggestions to improve the quality of this paper. We also acknowledge the anonymous referee. We acknowledge financial support from Spanish MINECO under grant AYA2014-29517-C03-01 and AYA2011-29517-C03-02. EJA acknowledges support from MINECO under grant AYA2013-40611-P. JMRE acknowledges support from MINECO under grant AYA2012-39168-C03-01. We acknowledge support from the Faculty of the European Space Astronomy Centre (ESAC). IRS acknowledges support from STFC GT/I001573/1, a European Research Council Advanced Programme Dustygal (321334) and a Royal Society/Wolfson Research Merit Award. Based on observations made with the Gran Telescopio Canarias (GTC), instaled in the Spanish Observatorio del Roque de los Muchachos of the Instituto de Astrofísica de Canarias, in the island of La Palma. This publication makes use of data products from the Two Micron All Sky Survey, which is a joint project of the University of Massachusetts and the Infrared Processing and Analysis Center/California Institute of Technology, funded by the National Aeronautics and Space Administration and the National Science Foundation.

-
- ¹ European Space Astronomy Centre (ESAC)/ESA, P.O. Box 78, 28690 Villanueva de la Canada, Madrid, Spain
e-mail: miguel.sanchez@sciops.esa.int
 - ² ISDEFE, Beatriz de Bobadilla 3, 28040 Madrid, Spain
 - ³ Instituto de Astrofísica de Canarias, E38205, La Laguna, Tenerife, Spain
 - ⁴ Universidad de La Laguna, Tenerife, Spain
 - ⁵ Instituto de Astrofísica de Andalucía, CSIC, Granada, Spain
 - ⁶ School of Physics and Astronomy, University of Nottingham, U.K.
 - ⁷ GEPI, Observatoire de Paris & CNRS, Meudon, France
 - ⁸ Centro de Astrobiología, INTA-CSIC, Madrid, Spain
 - ⁹ INAF, Osservatorio Astronomico di Trieste, Italy
 - ¹⁰ Department of Physics, University of Bristol, U.K.
 - ¹¹ Institut de Ciències de l'Espai (CSIC), Barcelona, Spain
 - ¹² Instituto Politécnico Nacional, México D.F., México
 - ¹³ Laboratoire AIM Saclay, CEA/IRFU, CNRS/INSU, Université Paris Diderot, France
 - ¹⁴ Department of Physics, McGill University, Montreal, Quebec, Canada
 - ¹⁵ Instituto de Física de Cantabria, CSIC-Univ. de Cantabria, Santander, Spain
 - ¹⁶ Departamento de Astronomía, Universidad de Chile, Casilla 36-D, Correo Central, Santiago, Chile
 - ¹⁷ University College, Belfield, Dublin, Ireland
 - ¹⁸ INAF, Osservatorio Astronomico di Padova, Italy
 - ¹⁹ Institute for Computational Cosmology, Durham University, Durham DH1 3LE, U.K.
 - ²⁰ Institute of Astro- and Particle Physics, University of Innsbruck, Austria
 - ²¹ Centro de Estudios de Física del Cosmos de Aragón, Teruel, Spain
 - ²² Dipartimento di Fisica, Università degli Studi di Milano, Milano, Italy
 - ²³ Dipartimento di Fisica, Università di Torino, Torino, Italy
 - ²⁴ Istituto Nazionale di Fisica Nucleare (INFN), sezione di Torino, Torino, Italy
 - ²⁵ Departamento de Astronomia, Instituto de Astronomia, Geofísica e Ciências Atmosféricas da USP, São Paulo, Brazil
 - ²⁶ Institute for Astronomy, University of Edinburgh, Royal Observatory, Blackford Hill, Edinburgh
 - ²⁷ European Southern Observatory, Garching, Germany
 - ²⁸ INAF-Osservatorio Astrofisico di Arcetri, Florence, Italy
 - ²⁹ Departamento de Astrofísica, Facultad de CC. Físicas, Universidad Complutense de Madrid, 28040, Madrid, Spain